This is a preprint, the final version is subject to change, of the American Mineralogist (MSA)
Cite as Authors (Year) Title. American Mineralogist, in press.
(DOI will not work until issue is live.) DOI: http://dx.doi.org/10.2138/am-2016-5532

Mineral chemistry and petrogenesis of a HFSE(+HREE) occurrence, peripheral to carbonatites of the Bear Lodge alkaline complex, Wyoming

Allen K. Andersen[1,*], James G. Clark[2], Peter B. Larson[1] and Owen K. Neill[1]
[1]School of the Environment, Washington State University, Pullman, WA 99164-2812, USA
[2]Applied Petrographics, 4909 NE 320 Ave., Camas, WA 98607

Abstract

Rare earth mineralization in the Bear Lodge alkaline complex (BLAC) is mainly associated with an anastomosing network of carbonatite dikes and veins, and their oxidized equivalents. Bear Lodge carbonatites are LREE-dominant, with some peripheral zones enriched in HREEs. We describe the unique chemistry and mineralogy one such peripheral zone, the Cole HFSE(+HREE) occurrence (CHO), located approximately 2 km from the main carbonatite intrusions. The CHO consists of anatase, xenotime-(Y), brockite, fluorite, zircon, and K-feldspar, and contains up to 44.88% TiO_2, 3.12% Nb_2O_5, 6.52% Y_2O_3, 0.80 % Dy_2O_3, 2.63% ThO_2, 6.0% P_2O_5, and 3.73% F. Electron microprobe analyses of xenotime-(Y) overgrowths on zircon show that oscillatory zoning is a result of variable Th and Ca content. Cheralite-type substitution, whereby Th and Ca are incorporated at the expense of REEs, is predominant over the more commonly observed thorite-type substitution in xenotime-(Y). Th/Ca-rich domains are highly beam sensitive and accompanied by high F concentrations and low microprobe oxide totals, suggesting cheralite-type substitution is more easily accommodated in fluorinated and hydrated/hydroxylated xenotime-(Y). Analyses of xenotime-(Y) and brockite show evidence of VO_4^{3-} substitution for PO_4^{3-} with patches of an undefined Ca-Th-Y-Ln phosphovanadate solid-solution composition within brockite clusters. Fluorite from the CHO is HREE-enriched with an average Y/Ho ratio of 33.2, while other generations of fluorite throughout the BLAC are LREE-enriched with Y/Ho ratios of 58.6-102.5.

HFSE(+HREE) mineralization occurs at the interface between alkaline silicate intrusions and the first outward occurrence of calcareous Paleozoic sedimentary rocks, which may be local sources of P, Ti, V, Zr, and Y. U-Pb zircon ages determined by LA-ICP-MS reveal two definitive $^{207}Pb/^{206}Pb$ populations at 2.60-2.75 Ga and 1.83-1.88 Ga, consistent with derivation from adjacent sandstones and Archean granite. Therefore, Zr and Hf are concentrated by a physical process independent of the Ti/Nb-enriched fluid composition responsible for anatase crystallization. The CHO exemplifies the extreme fluid compositions possible after protracted LREE-rich crystal fractionation and subsequent fluid exsolution in carbonatite-fluid systems. We suggest that the anatase+xenotime-(Y)+brockite+fluorite assemblage precipitated from highly-fractionated, low-temperature (<200°C), F-rich fluids temporally related to carbonatite emplacement, but after significant fractionation of ancylite and Ca-REE fluorocarbonates. Low temperature aqueous conditions are supported by the presence of fine-grained anatase as the sole Ti-oxide mineral, concentrically banded botryoidal fluorite textures, and presumed hydration of phosphate minerals. Fluid interaction with Ca-rich lithologies is known to initiate fluorite crystallization which may cause destabilization of (HREE,Ti,Nb)-fluoride complexes and precipitation of REE+Th phosphates and Nb-anatase, a model valuable to the exploration for economic concentrations of HREEs, Ti, and Nb.

Keywords: Xenotime, brockite, anatase, carbonatite, rare earth elements, HREE, fractionation, thorium

Introduction

Late-stage HREE enrichment is observed in a number of REE deposits/occurrences, many of which are related to carbonatite magmatism, including Lofdal, Namibia; Kalkfield and Ondurakorume complexes, Namibia; Juquiá, Brazil; Bayan Obo, China; Karonge, Burundi; and

the Barra do Itapirapuã carbonatite, Brazil, among others (Wall et al. 2008; Bühn 2008; Smith et al. 2000; Walter et al. 1995; Van Wambeke 1977; Andrade et al. 1999). Fractionation of the REEs will often result in zones enriched specifically in either LREEs (La-Gd) or HREEs (Tb-Lu and Y). This type of zoning may arise from crystal fractionation processes during magmatic stages, or from changes in the activity of ligands with which the REEs typically form aqueous complexes (i.e., Cl^-, F^-, CO_3^{2-}, SO_4^{2-}, and PO_4^{3-}) during hydrothermal stages.

Differences in the stability of these charged complexes with increasing atomic number of the trivalent REEs is a critical factor leading to fractionation (cf., Wood 1990a,b; Lee and Byrne 1992; Byrne and Li 1995; Wood 2003; Williams-Jones et al. 2012; Linnen et al. 2014). Hard bases such as F^- and CO_3^{2-} are most frequently cited as hydrothermal REE transport ligands, based largely on the stability of these REE complexes relative to complexes with ligands of intermediate hardness, like Cl^-, which are an order of magnitude lower (Schijf and Byrne 1999; Luo and Byrne 2001; Williams-Jones et al. 2012). Based on the thermodynamic data and stability constants of REE complexes available from studies by Wood (1990a,b) and Haas et al. (1995), $HREEF^{2+}$ complexes were predicted to be more mobile than $LREEF^{2+}$ complexes. New experimental work by Migdisov et al. (2009) shows that above 150°C, $LREEF^{2+}$ complexes are more stable than $HREEF^{2+}$ complexes, but that fluoride is an improbable transport ligand due to the low solubility of REE fluoride minerals (i.e., fluocerite) (Williams-Jones et al. 2012). REE-phosphate solubility equilibria have been investigated (cf., Jonasson et al. 1985; Firsching and Brune 1991; Bryne and Kim 1993; Liu and Byrne 1997; Cetiner 2003), but remain poorly understood beyond standard conditions (20-25°C; ~1.0 bar).

Yttrium is commonly referred to as a heavy pseudolanthanide because of its similar charge (3+) and radius to Ho^{3+}, and is appropriately placed between Dy^{3+} and Ho^{3+} on chondrite

normalized REE plots. In fluorine-rich systems, Y-Ho fractionation is common and recorded by high, non-chondritic Y/Ho ratios (>28.8, using C1 chondrite values of McDonough and Sun 1995) of hydrothermal fluorite (Bau and Dulski 1995; Loges et al. 2013). Variation of Y/Ho ratios in aqueous solutions is strongly influenced by temperature, fluoride activity, and differences in Y-fluoride *versus* REE-fluoride speciation (Loges et al. 2013). In natural fluorites, Y/Ho values between 50 and 200 are common (Bau and Dulski 1995; Bau 1996; Bau et al. 2003), and a similar range (33-103) is observed for Bear Lodge fluorites. REE concentrations (including Y) and chondrite-normalized REE patterns of fluorites sampled from different host-rock lithologies throughout the Bear Lodge alkaline complex (BLAC) are used to examine the behavior of REEs in late-stage hydrothermal fluids and identify separate stages of fluorite precipitation.

Changes in pH, redox, and dominant ligand may allow for extreme REE fractionation in late-stage, hydrothermal fluids associated with carbonatites. We investigate the possible scenario whereby HFSEs and HREEs are transported (possibly as fluoride or phosphate complexes) by fluids emanating from carbonatite intrusions, and precipitate as REE phosphates (xenotime-(Y) and REE-enriched brockite), fluorite, and anatase upon interaction with calcareous Paleozoic sedimentary rocks.

Within the REE-mineralized areas of the BLAC, the CHO is of particular economic interest because of its extraordinarily high concentrations of HREEs, Ti, and Nb. With the advancement of technologies utilizing HREEs and low abundance of HREEs relative to LREEs in the Earth's crust, xenotime is emerging as a potential source of the more valuable REEs (excepting Eu) in today's market. Xenotime is also becoming an increasingly useful mineral in geochemical and geochronological studies with in situ trace element and U-Pb isotopic analysis

by laser-ablation inductively coupled plasma mass spectrometry (LA-ICP-MS), secondary ion mass spectrometry (SIMS), and electron probe microanalysis (EPMA), and sensitive high resolution ion microprobe (SHRIMP). Understanding variations in actinide concentration and incorporation are important to the interpretation of ages determined by in situ methods. At the CHO, zones of variable actinide concentration in xenotime-(Y) are almost unequivocally related to the crystallization of brockite [$(Ca,Th)(PO_4)\cdot H_2O$], a member of the rhabdophane group. We present some of the most complete electron microprobe analyses of REE-enriched brockite and the first known analyses of a solid solution phase intermediate between brockite and a theoretical Th-Ca-Y-REE vanadate end-member.

Geologic Setting

The BLAC is a bilobate dome with an Eocene alkaline intrusive core, pendants or inliers of Archean granite/gneiss of the Wyoming Province, and a rim of outward dipping Paleozoic and Mesozoic sedimentary units (Fig. 1). The BLAC is part of a larger N70°W trend of Paleogene alkaline intrusive centers through the northern Black Hills region which represent the easternmost surface manifestations of Laramide-related magmatism. The transition between the Proterozoic Trans-Hudson suture zone and Wyoming Archean Province likely occurs 20-40 km east of the BLAC, and may have provided a zone of structural weakness that allowed for the ascension of mantle-derived alkaline silicate and carbonatite magmas.

Domal uplift of the BLAC occurred as alkaline silicate magmas intruded Paleozoic sedimentary units as sills and other small intrusive bodies, significantly inflating the sedimentary section (Dahlberg, 2014). Intermittent flux of alkaline magma continued through 38 Ma (McDowell 1971; Staatz 1983; Duke 2005), resulting in a central complex of small cross-cutting intrusions. The CHO occurs near a condensed section of the Cambrian-Ordovician Deadwood

Formation and Ordovician Winnipeg and Whitewood Formations, deposited near the edge of an Ordovician basin. Outcrops of the Deadwood Formation consist of well indurated quartz sandstone with interbedded black shales, calcareous siltstone, and probably more shale- and siltstone-dominant lithologies at depth. The Winnipeg Formation consists of the Roughlock Member (calcareous siltstone) and Ice Box Shale, while the Whitewood Formation consists of dolostone and interlayered limestone. The three formations are encountered along a ~20m traverse through historic trenches near the CHO. Similar depositional environments resulting in condensed sections of sandstone and shale, where high levels of dissolved phosphate are released into pore waters, are thought to be favorable sites for precipitation of coarse diagenetic xenotime (cf., Vallini et al. 2002).

Although the CHO occurs in close proximity to sedimentary rocks, a majority of the REE mineralization in the BLAC is associated with intrusions of calciocarbonatite (sövite) (and their oxidized equivalents) emplaced between 51 and 52 Ma (Andersen et al. 2013a). Staatz (1983) describes the BLAC as one of North America's largest "disseminated" rare earth deposits, although a majority of the potentially economic REE mineralization is "carbonatite-hosted." Carbonatite veins and dikes have been modified by late hydrothermal fluids and supergene processes that are responsible for high REE abundances. Extensive exploration between 2010 and 2014 has revealed zones of HREE-enrichment peripheral to the LREE-enriched center of the carbonatite dike swarm. The principal REE-bearing mineral in unoxidized carbonatite is ancylite [$Sr,Ln(CO_3)_2(OH)\cdot H_2O$] (Ln = lanthanide element(s)), with subordinate carbocernaite [$(Ca,Na)(Sr,Ln,Ba)(CO_3)_2$], burbankite [$(Na,Ca)_3(Sr,Ba,Ln)_3(CO_3)_5$], monazite [$Ln(PO_4)$], and apatite/fluorapatite [$Ca_5(PO_4)_3(F,OH)$] (Mariano 1981, 2009; Moore et al. 2014). REE-Ca fluorocarbonates (bastnäsite [$Ln(CO_3)F$], parisite [$Ca(Ln)_2(CO_3)_3F$], and synchysite

[$CaLn(CO_3)_2F$]) are the primary REE ore minerals in oxidized carbonatite equivalents, all of which are LREE-dominant. Zones of HREE-enrichment commonly coincide with an increase in the abundance of REE phosphates (rhabdophane group and xenotime) and HFSE minerals (rutile and pyrochlore) (Andersen et al. 2013b,c).

Site and Sample Descriptions

Description of the occurrence

The CHO is situated along the eastern edge of the BLAC near the easternmost exposures of alkaline silicate intrusions (Fig. 1). Rare earth mineralization appears to be restricted to the interface between quartz sandstone of the Deadwood Formation and greenish-gray clayshale and tan calcareous siltstone of the Winnipeg Formation. Several small intrusive bodies lie adjacent to, and in some cases appear to have brecciated, surrounding sedimentary units. Recrystallized quartz breccias commonly delineate these contacts and smoky quartz veins transect the quartz sandstones proximal to the CHO. The Cole HFSE(+HREE) mineralization was first described in detail by Staatz (1983) (*vein #22*) and confidential reports around the same time by Anthony N. Mariano. The exact dimensions of the occurrence are obscured by forest overgrowth and tailings from trenches and workings left from uranium exploration during the 1950s. Current exposures reveal what appear to be relatively flat-lying "veins" no more than 1 m thick. Small veinlets in surrounding brecciated alkaline silicate rock and siltstone are mineralogically similar to the more massive exposure. At least two other small areas of Th-REE phosphate mineralization occur in the western half of the BLAC at contacts between silicate or carbonatite intrusions and Paleozoic sedimentary rocks.

Sample mineralogy

The CHO differs both chemically and mineralogically from carbonatites and hydrothermal veins at Bear Lodge. In some oxidized carbonatite veins of the BLAC, phosphate minerals account for a majority of the HREE budget, but at the CHO only HREE-dominant phases (xenotime-(Y) and brockite) are present, with trace amounts of REEs in fluorite. The phosphorus-HFSE association at the CHO is similar to other sites peripheral to the central carbonatites. However, rutile/pseudorutile and pyrochlore group minerals are the predominant Ti- and Nb-bearing phases and fine-grained "supergene" monazite or rhabdophane are the principal REE-bearing phases at these peripheral localities. A definitive paragenesis of the CHO is difficult to establish, owing to complex textural relationships, the small grain size (typically <60 μm) of all phases except fluorite, and possible recrystallization. Except for inherited components (zircon and possibly K-feldspar), the CHO consists almost exclusively of anatase, xenotime-(Y), brockite, and fluorite, which appear to have crystallized in that sequence.

In the CHO, K-feldspar (30-40% modal) occurs as partially fragmented, 40-150 μm subhedral grains with corroded edges and coated with fine anatase druses. Detrital K-feldspar grains of similar size and morphology are found in adjacent sedimentary rocks, and are typically coated with authigenic K-feldspar overgrowths or interstitial cement. Rounded zircons (10-50 μm) are present in both the CHO and surrounding sandstone with zoning ranging from simple to complex. Zircon is volumetrically minor, but is much more abundant in the CHO compared to the sandstones.

Anatase is the most abundant mineral in CHO rocks (30-50% modal). The presence of anatase was confirmed by XRD and no other Ti-oxide minerals, including the anatase polymorph, rutile were found. In many environments anatase occurs as striated acute dipyramids, but here it occurs as more tabular crystals composed of a basal pinacoid with

numerous pyramidal faces (Fig. 2a). Crystals are oscillatory-zoned with 1-5 μm-wide bands of slightly irregular periodicity parallel to their faces. Anatase commonly occurs as thin bands of individual crystals precipitated on K-feldspar grain boundaries (Figs. 2b, 2c, 2d), acting as a cement. In some instances, anatase appears to nucleate on zircons with xenotime-(Y) outgrowths (Fig. 2e).

Brockite occurs as disseminated clusters of stubby hexagonal prisms (Fig. 2f) and cavity-lining druses (Fig. 2g). Textures indicate that brockite crystallization continued after xenotime-(Y) precipitation. A previously unrecognized, Th-Ca-Y-REE phosphovanadate phase occurs as irregular patches within some larger brockite clusters. At Bear Lodge, similar phosphovanadate phases were identified in oxidized carbonatite along with other rhabdophane group minerals, by the authors of this study.

Xenotime-(Y) occurs primarily as disseminated aggregates with individual crystals less than ~2 μm. It also occurs as minute, syntaxial, pyramidal or dipyramidal outgrowths (≤25 μm), or complete overgrowths (up to 80 μm), on rounded detrital zircon substrate (Figs. 2h and 2i). Zircon is a preferable host for xenotime-(Y) nucleation owing to their isostructural (tetragonal) relationship. This texture is observed in a variety of geological environments including carbonatites (e.g., Wall et al. 2008), hydrothermal veins, metamorphic rocks, granites (e.g., Corfu et al. 2003), and diagenetically altered sedimentary rocks (e.g., Rasmussen 1996, 2005). Both anatase and xenotime-(Y) are known to form well-developed, striated tetragonal dipyramids, but at the CHO, only xenotime-(Y), occurs in this form (Fig. 2h). Distinct compositional banding is apparent in BSE images of most large outgrowths (Figs. 2h and 2i). Phosphates, xenotime-(Y) and brockite represent ~10-20% of total CHO rock volume.

Xenotime-(Y) outgrowths of a distinctly different morphology occur in Cambrian-Ordovician quartz sandstone adjacent to the CHO (Figs. 2j and 2k). Sandstone-hosted xenotime-(Y) occurs as bulbous and serrated outgrowths with a porous microstructure similar to those documented by Hay et al. (2010). Xenotime-(Y) outgrowths in the Paleozoic section at Bear Lodge have remained unrecognized until this study, partly due to the metamict nature of xenotime-(Y) outgrowths, but also to the variable polishing procedures used for thin section preparation. One set of polished thin sections may contain abundant xenotime-(Y) outgrowths, while another may contain only the triangular-shaped voids left when outgrowths are dislodged during polishing (Fig. 2l). Xenotime-(Y) outgrowths occur on all zircons in the CHO and ~80% of zircons in the sandstone samples examined. In all CHO samples, fluorite (~3-10% modal) appears to be the final crystalizing phase, where it occurs as botryoidal, concentrically banded coatings lining cavities and small fractures (Fig. 2d).

Analytical Methods

SEM/EPMA imagining and analysis

REE phosphate mineral compositions were determined by wavelength dispersive electron probe microanalysis using a JEOL JXA-8500F field emission electron microprobe at Washington State University's GeoAnalytical Laboratory. The instrument was also used to generate backscattered electron (BSE) images. Additional BSE images were obtained using a FEI Quanta 200F field emission SEM housed at Washington State University's Franceschi Microscopy Center.

The fine-grained hydrated/hydroxylated REE phosphates present numerous analytical challenges, such as diffusive volatility of F (Goldstein et al. 1984; Pyle et al. 2002) and variable electon microprobe oxide totals due to the presence of significant unanalyzed H_2O or OH^-. The

fine-grained and potentially porous nature of these REE phosphates introduces additional uncertainty (commonly lower totals than predicted) compared to ideal samples required for high accuracy EPMA (Förster 2006; G□b et al. 2011). Various electron microprobe settings have been used to try and minimize crystal damage, volatility, and other potential sources of error, while still achieving precise measurement of REEs. Recent studies of hydrated REE minerals (e.g. Förster 2006; Krenn and Finger 2007; Berger et al. 2008; G□b et al. 2011) have used an accelerating voltage of 15-25 kV and beam current between 3 and 60 nA. Our test runs, completed using a range of beam conditions, showed little improvement in reducing the amount of damage at beam conditions as low as 15 kV and 15 nA, and slightly diminished precision. The small areas of homogeneous composition require a focused beam and increased counting time, which also contributes to mineral degradation during analysis. A defocused beam was used where crystal dimensions permitted. The presence of elements not included in the routine and submicron inclusions may also contribute to low totals and deviation from ideal stoichiometry. The most consistent data for the REE phosphates were generated using a 2-10 μm beam diameter, 20 kV accelerating voltage, and a 20-50 nA current. These conditions also allow for lower detection limits and analysis of REEs at low concentration, while maintaining reasonable analysis time.

A combination of natural and synthetic standards was used for calibration, including a set of synthetic REE orthophosphates. Preferred X-ray analytical lines were chosen based on the recommendations of Roeder (1985), Williams (1996), and Pyle et al. (2002). Background positions were chosen carefully to avoid spectral overlaps. Quantitative corrections using ProbeForEPMA software were made where overlaps could not be avoided (Donovan et al. 1993,

253 2007). Specific acquisition information and setup for REE phosphate analysis are presented in
254 Appendix Table 1.

255 **U-Pb geochronology and trace element analysis by LA-ICP-MS**

256 U-Pb age determination of zircon by LA-ICP-MS was performed at Washington State
257 University's GeoAnalytical Laboratory following procedures detailed in Chang et al. (2006).
258 Spot analyses of standards and unknowns were performed using a New Wave UP-213 laser
259 system with a spot size of 20 μm and a pulse rate of 10 Hz. Isotope ratios were measured on a
260 ThermoFinnigan Element2 single-collector HR-ICP–MS. An in-house zircon standard (Peixe),
261 with an established high precision TIMS age, was analyzed before and after a run of 20 unknown
262 sample grains and used to correct for mass, elemental, and instrument bias.

263 Data are reduced following the procedures of Chang et al. (2006). Signal intensities are
264 first corrected for background using blank measurements made prior to each analysis. To correct
265 for time-dependent mass and elemental fractionation of U and Pb, the U/Pb and Pb/Pb ratios of
266 standards are compared with the TIMS values to calculate fractionation factors, which are then
267 applied to unknown data. LA-ICP-MS can be used for U-Pb age determinations of xenotime;
268 however the fine-grained, heterogeneous nature of xenotime-(Y) in our samples precluded
269 analysis by this method.

270 Trace element concentrations in fluorite were performed on slide-mounted ~125 μm thick
271 sections and measured using the same LA-ICP-MS system used for U-Pb geochronology. For
272 the trace element routine, the laser was operated at 15 Hz with a 40-60 μm spot size. During trial
273 runs, greater precision was achieved from stationary spots rather than transects, although signal
274 decay was more severe as fluorite pitted under the laser. The systematic signal loss of all trace
275 elements was corrected using calcium concentration, which was obtained independently by

276 electron microprobe and used as an internal standard. Two concentration standards, NIST610
277 and NIST612, were ablated before and after unknown samples for external calibration. Specific
278 isotopes analyzed during LA-ICP-MS included: ^{88}Sr, ^{89}Y, ^{139}La, ^{140}Ce, ^{141}Pr, ^{146}Nd, ^{147}Sm, ^{151}Eu,
279 ^{160}Gd, ^{159}Tb, ^{163}Dy, ^{165}Ho, ^{166}Er, ^{169}Tm, ^{172}Yb, ^{175}Lu, ^{232}Th, and ^{238}U.

280 Controlled ablation of fluorite is often more difficult than other minerals owing to the
281 presence of inclusions and its perfect cleavage {111} in four directions, which may cause
282 uncontrolled flaking of large pieces from the mineral surface (Jackson et al., 1992). This results
283 in large particles entering the argon plasma and spikes in signal intensity which may result in
284 trace element data of questionable accuracy and precision. During our analyses, ablation
285 stabilized after an initial flaking of larger particles, which was unmistakable in the resulting
286 spectrum, and addressed during data reduction. Time intervals for the background, initial spike,
287 and signal region with uniform decay, were carefully selected. Any spectra with spikes,
288 indicating uncontrolled ablation or presence of inclusions, were excluded. Ratios of individual
289 REEs (e.g., La/Lu and Nd/Yb) were reviewed and remain consistent throughout the signal
290 region. Therefore, REE data are an accurate representation of the relative REE concentrations.

291 **Whole rock geochemistry**

292 Whole-rock compositions were determined at Activation Laboratories Ltd. using a
293 combination of techniques. Major and trace element concentrations were determined using a
294 lithium metaborate/tetraborate fusion with subsequent analysis by ICP-MS. The presence of
295 even low levels of phosphate are known to severely affect the ability to accurately measure
296 Nb_2O_5 by this method, with results biased toward low Nb_2O_5 values; therefore, Nb_2O_5, ZrO_2, and
297 Ta_2O_5 were reanalyzed by fusion XRF. A second trace element analysis included an aqua regia
298 digestion followed by ICP-MS for chalcophile elements known to volatilize (i.e., Sb, As, Mo,

299 Ga, Zn) during the fusion process. Reduced iron was measured by titration, and sulfur species
300 were determined by infrared methods. Fluorine was analyzed by ion selective electrode and CO_2
301 by coulometry.

302 ## Results and Discussion

303 ### Whole-rock geochemistry

304 Results from whole-rock analysis of three CHO vein samples and potential
305 HFSE(+HREE) source rocks are presented in Appendix Table 2. Unlike LREE-enriched, HFSE-
306 poor carbonatite intrusions at the center of the BLAC, the CHO is enriched in Be, F, P, Se, Sn,
307 and nearly all HFSEs and HREEs, with Y and lanthanides heavier than Tb representing 95% of
308 all REEs. Normalized to a composite of nine unoxidized Bear Lodge carbonatite samples, rocks
309 of the CHO are depleted in Ba, Pb, Sr, and La-Sm, and enriched in most trace elements with an
310 ionic potential greater than that of Gd (Fig. 3a). These results are consistent with the abundance
311 of xenotime-(Y) and brockite and absence of calcite in CHO rocks compared with the high
312 modal abundance of calcite, ancylite and Ca-REE fluorocarbonates in the central carbonatites.
313 Local Paleozoic sedimentary rocks and phonolitic intrusions have similar LILE and LREE
314 concentrations compared with the CHO, but chondrite normalized trace element patterns for the
315 CHO deviate from these lithologies for all HFSEs and REEs heavier than Nd (Fig. 3b).

316 Concentrations of HREEs and HFSEs in rocks of the CHO are in general, 2-3 orders of
317 magnitude greater than local Paleozoic sediments, alkaline silicate intrusions, and carbonatites.
318 TiO_2 concentrations are ~24.0-44.0 wt% higher and Nb_2O_5 1.8-3.1 wt% higher than other
319 lithologies owing to the high modal abundance of anatase. Nb/Ti ratios are ~1-3 orders of
320 magnitude greater than local Paleozoic sediments and more comparable to Nb/Ti ratios of
321 carbonatite and alkaline silicate intrusions (Appendix Table 2). In CHO rocks, thorium and

vanadium reach 3430-26300 ppm and 11430-16170 ppm, respectively. The adjacent Icebox clayshale (#25172) with 1320 ppm vanadium and carbonatites with an average of 467 ppm thorium are potential source rocks of these HFSEs, although concentrations are still an order of magnitude lower than CHO rocks. Except for Zr and Hf, alkaline silicate intrusions (e.g. phonolite dike sample #12BL24) and carbonatites of the BLAC have similar HFSE concentrations.

Mineral chemistry from EDS, EPMA, and LA-ICP-MS

Brockite. Brockite [$(Ca,Th,Ln)(PO_4)\cdot H_2O$] is a rare mineral found only in a few localities associated with metamorphosed quartz sandstones, granites and granite pegmatites, and Th-REE carbonatites, typically forming as secondary alteration product of thorite (Fisher and Meyrowitz 1962; Tiegeng et al. 1987; Shoji and Akai 1994; Berger et al. 2008). No precursory thorite or other Th-bearing phases are identified at the CHO, suggesting direct precipitation from Th-rich solutions. CHO brockite analyses are compared with the initial chemical analyses of brockite from Th-REE carbonatite veins of the Wet Mountains, Colorado by Fisher and Meyrowitz (1962). More recent analyses (Tiegeng et al. 1987; Shoji and Akai 1994; Berger et al. 2008), are all LREE-dominant varieties, although complete REE analyses are not always attempted. Chondrite normalized REE patterns of brockite from the CHO are roughly parallel to those of brockite analyzed by Fisher and Meyrowitz (1962) (Fig. 4), but CHO brockite is HREE-dominant, with greater concentrations of REEs heavier than Tb and 3.2-5.2 wt% Y_2O_3 (Table 1a). To the authors' knowledge, brockite from the CHO contains the highest reported concentrations of REEs. Although there is significant variability in REE, Th, and Ca content, REEs are incorporated into brockite according the substitution mechanism also responsible for miscibility between monoclinic monazite and cheralite (Gramaccioli and Segalstad 1978; Watt

1995; Chakhmouradian and Mitchell 1998; Förster 1998a; Linthout 2007) and often referred to as "brabantitic" or "cheralitic" substitution (Fig. 5a):

$$2(Y, REE)^{3+} = (Th, U)^{4+} + Ca^{2+} \quad (1)$$

Although reasonably pure separations for verification by XRD were unsuccessful, brockite is identified based on its hexagonal form (Fig. 2f) and Th- and Ca-dominant composition determined by EPMA (Table 1a). Staatz (1983) lists brockite as a mineral confirmed by XRD at the CHO. Similar species include end-member cheralite [$Ca,Th(PO_4)_2$], churchite-(Y) [$YPO_4 \cdot 2H_2O$], and grayite [$(Th,Pb,Ca)(PO_4) \cdot H_2O$], another member of the rhabdophane group. Chemical analyses of end-member cheralite are often indistinguishable from brockite, lending some uncertainty to identifications based on chemistry alone. Electron microprobe totals for brockite should be lower than those of end-member cheralite, owing to the presence of H_2O.

Microprobe oxide totals for CHO brockite average 88.4%, which is close to the expected value when accounting for the theoretical ~8 wt% H_2O in brockite. Our analyses of brockite include 0.64-1.69 wt% F, while no previously reported analyses have included F. This suggests that brockite may include hydroxyl rather than molecular water, or both. Incorporation of F^- and OH^- would also help correct for the observed charge imbalance as a result of excess REEs. Trace amounts of CO_3^{2-}, not analyzed, may also contribute to the low electron microprobe oxide totals, as chemical analyses by Tiegeng et al. (1987) and Fisher and Meyrowitz (1962) contain 2.55 and 3.1 wt% CO_2 (0.15 and 0.17 CO_3 *apfu*), respectively.

Undefined (Ca,Th,Y,Ln)[(V,P)O4]·nH$_2$O. In phosphate minerals, substitution of VO_4^{3-} and AsO_4^{3-} ions for PO_4^{3-} is often reported, and in some cases, complete solid-solution between

367 PO_4- and VO_4-rich end members is suspected. Complete miscibility between xenotime-(Y)
368 [YPO_4] and wakefieldite-(Y) [YVO_4] is suspected, although poorly understood (Kolitsch and
369 Holtstam 2004; Hetherington et al. 2008). The existence of an intermediate member of this
370 series [$Y((V,P)O_4)$] was encountered in oxidized carbonatite of the BLAC by the authors of this
371 study. Substitution of Nb is also possible, with fergusonite ($YNbO_4$) as the end member
372 composition. However, all Nb appears to partition into anatase at the CHO.
373 Hydrated/hydroxlated Ca-Th-Y-Ln phosphovanadate at the CHO probably represents an
374 intermediate composition between brockite [$(Ca,Th,Ln)(PO_4)\cdot H_2O$] and a theoretical V-dominant
375 end member [$(Ca,Th,Ln)(VO_4)\cdot H_2O$].
376 The Ca-Th-Y-Ln phosphovanadate phase occurs as irregular patches (possible
377 exsolution) within brockite clusters (Fig. 6a). It appears as the brightest phase (highest average
378 atomic #) in BSE images owing to Th and V concentrations higher than all other minerals.
379 Electron microprobe data show the new phase has slightly higher V than P, and higher Th/Ca
380 ratios compared with brockite (Table 1b). Chondrite-normalized REE patterns are nearly
381 identical to those of brockite, with slightly higher HREE contents, and the phase is interpreted
382 simply as *vanadatian brockite*.
383 The newly discovered phase may account for a substantial amount of the 1.37 wt%
384 average V concentration from whole rock analyses; however, the completely exsolved
385 phosphovanadate is not particularly abundant. Brockite, from which the secondary
386 phosphovanadate phase has not exsolved, and xenotime-(Y) account for a majority of the V
387 budget. Brockite actually contains less V than co-existing xenotime-(Y), suggesting removal of
388 V as it partitioned into the phosphovanadate phase. The undefined Ca-Th-Y-Ln phosphovanadate
389 phase, or one chemically similar, was first discovered by the authors in oxidized carbonatite

nearly 2 km from the CHO, where it occurs as micron-size acicular needles among other minerals of the rhabdophane group.

Although no official name is designated for a hydrated/hydroxlated Ca-Th-Y-Ln phosphovanadate, chemically similar phases have been described previously. Hydrated thorite analyses of Lumpkin and Chakoumakos (1988) are similar to our Ca-Th-Y-Ln phosphovanadate, although the authors claim that all samples possess the tetragonal zircon structure with lattice constants similar to thorite (Lumpkin and Chakoumakos 1986, 1988). Brown "thorite" samples from a cleavlandite unit (Lumpkin and Chakoumakos 1988: *Tables 1 and 2*) contain up to 16.2 wt% V_2O_5 and 19.5 wt% P_2O_5, which predominate over Si and As. These VO_4/PO_4-dominant "thorites" also exhibit high F concentrations (0.52-1.60 wt%) and the lowest oxide totals (~89-92%), which suggest that the incorporation of V and P is accompanied by a greater degree of hydration (and fluorination) than for Si-dominant varieties. Phosphate minerals of the CHO lack any appreciable Si, and the association with hexagonal brockite suggests our hydrated/hydroxlated Ca-Th-Y-Ln phosphovanadate phase is more closely related to the rhabdophane group.

Xenotime-(Y). Overgrowths of xenotime-(Y) on zircon in the CHO are structurally and chemically complex, with narrow zones which are highly beam sensitive (Fig. 6b). While Y^{3+} is the predominant A-site cation (average Y_2O_3: ~39 wt%), xenotime-(Y) contains an appreciable amount of other REEs averaging 13.1 wt% total rare earth oxide (TREO) (Table 2). Beam sensitive zones are enriched in Th and Ca, and deterioration under the electron beam is probably due to the presence of H_2O or OH^-, a feature not commonly reported for xenotime-(Y). Thorium is typically incorporated into xenotime-(Y) according to the charge-compensating substitution (van Emden et al. 1997; Förster 1998b):

413 $$(Th, U)^{4+} + Si^{4+} = (Y, REE)^{3+} + P^{5+} \quad (2)$$

414 The predominance of mechanism 2, involving coupled substitution of Th and Si in
415 xenotime-(Y), is not surprising, considering the isostructural relationship of thorite ($ThSiO_4$) and
416 xenotime-(Y). However, in CHO xenotime-(Y), Th, U, and Ca are incorporated according to
417 cheralite-type substitution (mechanism 1, Fig. 5b) with an accompanying decrease in P and
418 increase in F (and possibly OH) (Figs. 5c, 5d).
419 The Th- and Ca-rich bands normal to the c-axis of pyramidal xenotime-(Y) overgrowths
420 appear darker than the more pure xenotime-(Y) component in BSE images (Figs. 2h, 2i, 6b–e).
421 Substitution of Th should increase the average atomic number of xenotime-(Y), and it is
422 improbable that the coinciding substitution of Ca would bring down the average atomic number
423 to produce the dark banding in xenotime-(Y). We propose that incorporation of H_2O/OH^-, along
424 with Th and Ca, is responsible for the darker banding in xenotime-(Y). This is supported by the
425 micro-porous texture and extremely beam sensitive nature of the Th/Ca-rich bands (Fig. 6b).
426 The exact mechanism by which water is incorporated into xenotime-(Y) is unclear, but
427 incorporation of Th, Ca, and water together suggests an association with brockite crystallization.
428 Chondrite-normalized REE patterns for xenotime-(Y) and brockite are rough reflections of one
429 another for Tb-Lu (Fig. 7). Profiles of brockite show an Y-depletion relative to adjacent Dy and
430 Ho, which is probably a result of preferential Y-partitioning into xenotime-(Y) and fluorite, both
431 of which show positive Y-anomalies. The mirrored chondrite normalized patterns, Th/Ca-rich
432 domains in xenotime-(Y), and fine intergrowths of xenotime-(Y) and brockite in disseminated
433 clusters support co-precipitation of the two phases. Incorporation of Th and Ca also appears to
434 coincide with exchange in the tetrahedral site, where higher V concentrations are observed in
435 Th/Ca-rich domains (Fig. 5e). Where bright, low-water bands were sufficiently large to allow

436 analysis by electron microprobe, more typical, near stoichiometric xenotime-(Y) compositions
437 were obtained, with an average of 9.5 wt% higher Y_2O_3, 4.0 wt% higher P_2O_5, higher HREEs,
438 and lower Th, Ca, and V (Table 2). Xenotime-(Y) from albitites at Lofdal, Namibia, have lower
439 concentrations of Th, Ca, V, and F more typically observed for xenotime-(Y) and were analyzed
440 using the same routine as a check on accuracy (Appendix Table 4).

441 Variations of Th, U, Ca, and Si in xenotime-(Y) are commonly manifested in the form of
442 crystallographic and/or fine-scale (<5 μm) compositional zoning and additional variations in
443 actinide content may arise in during alteration and metamictization (Kositcin et al. 2003;
444 Rasmussen 2005; Vallini et al., 2005; Harlov and Wirth 2012). The Th and Ca variations in
445 CHO outgrowths can probably be attributed to successive phases of xenotime-(Y) precipitation
446 from a fluid with fluctuating Th and Ca concentrations, influenced by the simultaneous
447 precipitation of brockite. Subsequent alteration and partial dissolution/reprecipitation may have
448 also affected xenotime-(Y) composition. Outgrowth banding is commonly disrupted adjacent to
449 the zircon substrate (Fig. 6c–e), but remains as uniform banding further from the zircon
450 boundary toward pyramidal terminations. This indicates a possible hiatus in growth of syntaxial
451 xenotime-(Y) marked by partial dissolution of early adjacent xenotime-(Y) and in some
452 examples, anatase inclusions (Fig. 6e). There is clear evidence that the beam-sensitive Th/Ca-
453 rich domains were preferentially affected by later fluids (Fig. 6c), and in some cases fissures of
454 recrystallized xenotime-(Y) transect the uniform outer banding (Fig. 6d). Regardless of the exact
455 timing, xenotime-(Y) closest to the zircon substrate became slightly more soluble and susceptible
456 to dissolution/reprecipitation by later fluids.

457 While the many substitutions possible in xenotime-(Y) and hydrated/fluorinated REE+Th
458 phosphates are beyond the scope of this study, analyses of CHO xenotime-(Y) are consistent

459 with other studies of xenotime-(Y) which show significant deviation from ideal stoichiometry
460 (cf., Johan and Johan 2004; Förster 2006; Bastos Neto et al. 2012). Such deviations typically
461 involve B-site (Si, P) deficiencies and an excess of A-site cations (Th, Ca, Ln, Y) (Forster,
462 2006), as observed in CHO xenotime-(Y). Bastos Neto et al. (2012) suggest that the
463 development of PO_3F tetrahedra may be important in F-rich xenotime-(Y) from the Madeira
464 granite at Pitinga, Brazil. A similar substitution involving F^-/OH^- and H_2O is employed to
465 explain low microprobe oxide totals of xenotime-(Y) from the Cínovec (Zinnwald) granite
466 cupola in the Czech Republic, with the general formula, $[(Y, REE)_{1-x}\square_x]\ [(P, Si)O_{4-3x}(OH,F)_{3x}] \cdot$
467 $1\text{-}2H_2O$ (Johan and Johan 2004). The mechanism, $[(Th, U, Zr)_{1-x}\ (Y, REE)_x]\ [(SiO_4)_{1-x}(OH,F)_{3x}]$
468 is recognized for isostructural silicate members, thorite, zircon, coffinite, and thorogummite
469 (Pointer et al. 1988; Förster 2006). Substitutions of this type probably account for the
470 anomalously high F concentrations (1.96-3.02 wt%, Table 4), negative correlation between P and
471 F (Fig. 5d), and low microprobe oxide totals (81.2-96.2 wt%) of CHO xenotime-(Y). In
472 xenotime where Th and Si are introduced according to mechanism 1 (thorite-type), charge
473 balance appears to be maintained through the substitution $O^{2-} + P^{5+} = (F,OH)^- + Si^{4+}$ (Bastos
474 Neto et al. 2012). However, the extraordinarily F-rich xenotime-(Y) at both the CHO and
475 Madeira granites are notably poor in Si. Bastos Neto et al. (2012) suggest that unit cell
476 contraction related to the formation of PO_3F tetrahedra may inhibit replacement of P (0.17Å) by
477 Si (0.26Å.), thus explaining the poor effectiveness of thorite-type substitution in F-rich
478 xenotime-(Y) and B-site (P) vacancies in order to achieve charge balance. This may enable
479 cheralite-type substitution in F(±OH)-rich xenotime-(Y) like that of the CHO. An additional
480 factor controlling actinide incorporation is the availability of charge balancing Si^{4+} versus Ca^{2+},
481 as suggested by Förster (1998b). The lack Si-bearing hydrothermal minerals at the CHO and

high Ca^{2+} activity indicated by fluorite mineralization in the vicinity of calcareous sediments lends support this conclusion.

Sandstone-hosted xenotime-(Y). REE concentrations and chondrite-normalized patterns of quartz sandstone-hosted xenotime-(Y) outgrowths are nearly indistinguishable from the complex zoned overgrowths at the CHO (Table 2, Fig. 7). Sandstone outgrowths have slightly higher Nd and lower Th, Ca, V, and F. Excess SiO_2 is probably a result of the beam excitation volume overlapping onto the zircon substrate or adjacent quartz during analysis of outgrowths <5 μm. Although sandstone-hosted xenotime-(Y) has a radically different morphology compared to CHO xenotime-(Y) (compare Figs. 2j, 2k and Figs. 2h, 2i), the nearly identical compositions support a single generation of xenotime-(Y) precipitation. Th and F concentrations are only slightly lower compared to CHO xenotime-(Y) and are higher than most diagenetic xenotime-(Y) analyses reported in the literature. The contrast in morphology and absence of compositional (Th and Ca) zoning in sandstone-hosted outgrowths can be explained by the impediment of xenotime-(Y) growth by closely packed quartz grains in the indurated sandstone.

The metamict nature of xenotime-(Y) suggests outgrowths would not survive mechanical abrasion during transport of zircon, whether concentrated by gravity separation as in a placer-type occurrence or by hydrothermal fluids. The bond between xenotime-(Y) outgrowths and their detrital zircon substrate is not particularly strong (Rasmussen, 2005), yet dislodged pyramidal xenotime-(Y) fragments are rare within the CHO, indicating xenotime-(Y) outgrowths formed in situ and are not derived from the sandstones. Furthermore, outgrowths on zircon represent only a small percentage of the overall xenotime-(Y) in rocks of the CHO. A majority

504 of the xenotime-(Y) occurs as disseminated crystal clusters which are not present in the adjacent
505 sandstones.

506 Two separate generations of xenotime-(Y) precipitation (CHO vs adjacent quartz
507 sandstone) cannot be excluded on the basis of morphology and composition alone. Sandstone-
508 hosted xenotime-(Y) may represent phosphate mineralization from pore waters during diagenesis
509 (Rasmussen and Glover 1994, 1996; Rasmussen 1996, 2005; Hay et al. 2010), or a low-
510 temperature metamorphic event (Vallini et al. 2002, 2005), which may predate Paleogene
511 carbonatite-related REE mineralization by as much as 400 million years. Further
512 geochronological studies are required to distinguish between a predominantly Cambrian-
513 Ordovician diagenetic or Paleogene hydrothermal origin for xenotime-(Y), but are complicated
514 by morphology and actinide mobility.

515 **Fluorite.** While the REE content of fluorite from the CHO is significantly lower than
516 that of the phosphate minerals, it has a remarkably similar lanthanide distribution. CHO fluorite
517 is HREE-enriched with a chondrite-normalized REE maximum at Y and minimum at Nd. This
518 REE distribution is strikingly different from LREE-dominant fluorite in Bear Lodge carbonatite
519 dikes, hydrothermal veins, and limestone karst cavities (Table 3, Fig. 8). Fluorite from the CHO
520 is further distinguished by its lack of Y-Ho fractionation, indicated by low Y/Ho ratios, and the
521 absence of a negative Eu anomaly. Contrasts in the behavior of Y and Ho have been attributed
522 to their different outer electron configurations, mass-dependent fractionation, and temperature-
523 dependent fractionation (Olin and Wolff 2010, 2012 and references therein). Element
524 fractionations are in general expected to be more pronounced at lower temperatures, as noted by
525 Bau (1996, 1999) and Bau and Dulski (1999). In fluorite specifically, Y-Ho fractionation has
526 been attributed to different dominant speciation between Y-fluoride (di-fluoride) and REE-

fluoride (monofluoride) complexes in F-rich fluids at temperatures up to 250°C, as opposed to a source related phenomenon (Bau and Dulski 1995; Loges et al. 2013). The REE pattern of late void-filling fluorite at the CHO (Fig. 8) reveals the HREE-enriched/LREE-depleted composition of the fluid through the xenotime-brockite-fluorite sequence, consumption of phosphorus, and probable increase in fluorine. While Y is preferentially partitioned into fluorite relative to Ho, both are preferentially partitioned into xenotime-(Y). Crystallization of the less soluble REE+Th phosphates would significantly decrease Y and Ho concentrations and affect the Y/Ho ratio in the residual fluid. The lower Y/Ho ratios of CHO fluorite relative to all other fluorite at the BLAC is probably related to the fractionation of xenotime-(Y), which is rare in the central carbonatite dikes and other areas of fluorite mineralization. Based on the observed textures, mineral parageneses, and studies of Y-Ho fractionation in fluorine-rich fluids (e.g., Loges et al. 2013), fluorine activity, temperature, and pH were probably the most important factors contributing to Y-Ho variability in Bear Lodge fluorites. The preferential incorporation of Y into fluorite is probably responsible for the circular Y soil anomaly rimming the BLAC (Fig. 9). The Y anomaly appears to define fluorite-filled karst cavities in the Mississippian Pahasapa (Madison) limestone, some of which were mined ~0.5 km outward from the CHO.

Anatase. WDS X-ray element mapping and EDS point analyses indicate anatase zoning revealed in BSE images is due to variations in Nb concentration. Assuming all Ti and Nb have partitioned into anatase, the ratio of Nb to Ti in whole-rock analyses suggest the formula of anatase is close to $Ti_{0.92}Nb_{0.08}O_2$. Niobium, which substitutes for Ti^{4+} in 6-fold coordination, accounts for all 1.88-3.11 wt% Nb_2O_5 in CHO samples. Although the rutile structure is denser than the anatase structure, the octahedral coordination site around Ti^{4+} is larger in rutile, allowing Nb to be more easily accommodated in this structure, rather than anatase (personal

550 communication, Anthony N. Mariano). This may indicate that temperature was the controlling
551 factor that favored anatase (low-T TiO_2 polymorph) crystallization over rutile.

552 In sandstones and heavy mineral sands, anatase occurs as a detrital or authigenic
553 (diagenetic) mineral, commonly forming overgrowths or acting as a cement (Force, 1991; Ixer et
554 al. 1979; Ixer and Vaughan 1982; Morad and Aldahan 1982; Selleck 2008; Selleck et al. 2008).
555 The source of authigenic anatase is usually attributed to TiO_2 liberated from detrital ilmenite,
556 rutile, anatase, titanite, or biotite during diagenesis. The morphology and cement-like texture of
557 CHO anatase indicate an "authigenic" origin, in the sense that anatase formed in situ by
558 precipitation from fluids, but not necessarily a "diagenetic" origin as local quartz sandstones do
559 not contain significant quantities of detrital Fe-Ti oxides. Shales are known to have even higher
560 concentrations of TiO_2 (~0.6-1.0 wt%), which Force (1991) attributes to fine-grained anatase
561 commonly present in regoliths and derived from weathering of Ti-bearing silicate or oxide
562 minerals. Shales of the mid-upper Deadwood Formation and the Icebox clayshale of the
563 Winnipeg Formation could be local sources of TiO_2. However, a maximum concentration of
564 ~0.9 wt% TiO_2 was determined for the Icebox clayshale (Appendix Table 2), which would
565 appear to be an insufficient source of TiO_2 without extremely high water:rock ratios through this
566 relatively narrow unit.

567 **U-Pb geochronology of zircon by LA-ICP-MS**

568 The trace element chemistry of xenotime-(Y), brockite, and fluorite and euhedral
569 morphology of cement-forming anatase suggest these phases are genetically related to a
570 HREE(+HFSE)-enriched hydrothermal fluid. This assemblage accounts for nearly all REEs and
571 HFSEs, except Zr and Hf, which are hosted almost exclusively by zircon. U-Pb ages of CHO
572 zircons were determined by LA-ICP-MS to confirm that Zr and Hf were introduced by a physical

process independent of the HFSE-enriched fluid composition. Three distinct age populations are recorded by zircon xenocrysts (Table 4). The three Archean $^{207}Pb/^{206}Pb$ ages at 2.75-2.60 Ga are typical for granites of the Wyoming craton, and correspond with periods of calc-alkaline arc magmatism and penetrative deformation recorded in the Sweetwater subprovince in central Wyoming, and along the southern margin (Southern accreted terranes) of the older Wyoming craton (2.90-2.75 Ga) (cf., Chamberlain et al. 2003; Frost and Fanning 2006; Mueller and Frost 2006). The six Paleoproterozoic ages at 1.88-1.83 Ga (Table 4) are consistent with the Trans-Hudson Orogen during Hearne-Medicine Hat-Superior convergence in central Canada, and reported ages for xenoliths and granitic rocks of the Great Falls tectonic zone (Highwood and Little Belt Mountains), northwest of the Wyoming craton (Carlson and Irving 1994; Rudnick et al. 1999; Mueller et al. 2002; Vogl et al. 2002). Three of the six grains with $^{207}Pb/^{206}Pb$ ages at 1.88-1.83 Ga are highly discordant (CF7100V-14, CF7100V-15, CF7100V-24), which is probably a result of radiogenic Pb loss during the local Paleogene magmatic-hydrothermal event.

Ages between 1.8 and 1.9 Ga, and local influence of the Trans-Hudson Orogen are reasonably expected, considering the inferred boundary of the Trans-Hudson Suture Zone is approximately 20 km east of the BLAC. However, there is little evidence of a ca. 1860-1845 Ma or 1825-1790 Ma thermotectonic event in the western Dakotas region aside from ~1845-1810 Ma total-Pb ages of in situ monazite growth in metapelites of the Black Hills (Dahl et al. 1999, 2005a, 2005b). Instead, this area appears to have been affected by a distinctly younger (1800-1700 Ma) event (Black Hills orogeny), which postdates terminal Hearne-Superior collision in the northern Trans-Hudson Orogen and is contemporaneous with the Wyoming-(Dakota)-Superior cratonic collision and N-NW directed accretion along the southern Wyoming craton margin (Sims and Peterman 1986; Bickford et al. 1990; Dahl and Frei 1998; Dahl et al. 2005b). To our

596 knowledge, there are an insufficient number of U-Pb ages for Archean granite-hosted zircon
597 from the BLAC to determine whether the granites recorded either the 1.9-1.8 Ga Trans-Hudson
598 or 1.8-1.7 Ga Black Hills orogenic events.

599 Three older Paleoproterozoic ages at 1.97-2.11 Ga, recorded by zircons of the CHO,
600 would predate the Trans-Hudson Orogen and are probably the result of inherited ~2.7-2.6 Ga
601 zircon cores and ~1.9-1.7 Ga rims unresolved due to limited spatial resolution during analysis by
602 LA-ICP-MS. Alternatively, this age may represent a separate zircon population or overgrowth
603 domain related to a period of craton-wide extension and continental rifting indicated by 2.1-2.0
604 Ga mafic dike swarms exposed in the Wind River Range, Granite Mountains, and Laramie
605 Mountains (Cox et al. 2000; Chamberlain et al. 2003; Frost and Fanning 2006).

606 The two definitive $^{207}Pb/^{206}Pb$ age populations at 2.60-2.75 Ga and 1.83-1.88 Ga, and
607 lack of relict Trans-Hudson dates in the Black Hills concurrent with the latter, suggest
608 xenocrystic zircons of the CHO were derived from surrounding Cambrian-Ordovician quartz
609 sandstones, either being dislodged by fluids which precipitated HREE- and HFSE-bearing
610 minerals, or by gravity separation during transport and formation of a placer-type deposit. Its
611 abundance in CHO rocks suggests that zircon was preferentially and mechanically removed
612 (possibly with K-feldspar) by a fluid in which quartz was soluble, as rocks of the CHO contain
613 no quartz. Selective incorporation of zircon with no other xenocrystic component is improbable,
614 and the fragmented nature of K-feldspar suggests its incorporation concomitantly with zircon.
615 Although the CHO is enriched in nearly all HFSEs, the radiogenic U-Pb isotope analyses show
616 that Zr and Hf were enriched due to a mechanical concentration of zircon, physiochemically
617 independent of the Ti-Nb, Th-Y-P, and F mineralization.

618 **Source of HFSEs and HREEs and constraints on fluid chemistry**

The HREE-enrichment patterns of brockite, xenotime-(Y), and fluorite suggest that all three phases precipitated from the same chemically unique fluid. The high TiO_2 concentrations, predominance of HREE-dominant phosphates, and low Y/Ho ratios of CHO fluorite, suggest fluids of significantly different chemistry are responsible for mineralization at the CHO compared with other distinct episodes of hydrothermal REE mineralization (i.e., Ca-REE fluorocarbonate mineralization in the oxidized carbonatites) in the BLAC. Parameters such as temperature, pH, and host rock lithology may also have influenced the resulting REE assemblage. Although quite limited, the following observations suggest a link between hydrothermal mineralization at the CHO and the central Bear Lodge carbonatites:

1) REE mineralization: Although a majority of the REE mineralization in carbonatites is represented by carbonates and fluorocarbonates, oxidized portions contain REE phosphates of the rhabdophane group, including brockite. The abundance of REEs in general support a link between REE-rich carbonatites and the CHO, although significant fractionation of the REEs is required. The trace amounts of xenotime-(Y) and monazite in sedimentary rocks at Bear Lodge may be of diagenetic rather than carbonatitic/hydrothermal origin, but appear to be an insufficient source of REEs.
2) Th concentration: Geochemical mapping based on thousands of surface rock and soil samples and drill core assays clearly shows that Paleogene alkaline intrusions (carbonatites specifically) are the principal source of elevated Th at Bear Lodge (communication, Jeffrey Jaacks, Geochemical Applications International, Inc.; John Ray, Rare Element Resources, Ltd.). The unoxidized carbonatite samples analyzed during this study have an average Th concentration of 467 ppm (Appendix Table 2). A second and

641 completely unrelated source for the 0.34-2.63 wt% Th in the CHO would be an
642 extraordinary coincidence.

643 Furthermore, we suggest that the concentration of HREEs in a residual fluid may be the result of
644 fractional crystallization and selective removal of LREEs in REE-carbonates and
645 fluorocarbonates within the central carbonatite dike swarm. La, Ce, Pr, and Nd are at or below
646 detection limits for xenotime-(Y), brockite, and fluorite, suggesting fluids were impoverished in
647 LREEs before reaching sedimentary units ~2 km outward from the carbonatites.

648 If CHO minerals are indicative of HFSE and HREE transport in a F-rich hydrothermal
649 fluid, then the phosphatic shales and calcareous siltstones may have supplied the required Ca and
650 P to promote fluorite and REE phosphate precipitation. Fluorite crystallization may destabilize
651 HREE- and HFSE-fluoride complexes, resulting in deposition of xenotime-(Y), brockite, and
652 anatase. Destabilization of HFSE-fluoride complexes as a result of fluorite crystallization is a
653 suggested model for Zr-Y-Nb-REE mineralization in some peralkaline igneous complexes (Salvi
654 and Williams-Jones 1996, 2005). The sedimentary units exposed near the CHO are the first Ca-
655 rich lithologies moving outward from the central carbonatites, which might explain how HFSEs
656 and HREEs could remain in solution until fluorite saturation. Interaction of oxidizing fluids with
657 reduced lithologies is an alternative mechanism known to promote precipitation of hydrothermal
658 minerals, and shales near the CHO, with slightly more pronounced negative Eu anomalies, are
659 indicative of such conditions.

660 Secondary hydrated Ca-phosphate and -vanadate minerals such as sincosite
661 [$CaV_2(PO_4)_2O_2 \cdot 5H_2O$] and phosphovanadylite-Ca [$Ca(V_4P_2O_{12}(OH)_4) \cdot 12H_2O$] are not
662 uncommon in phosphatic and black carbonaceous shales. The chemical similarity of these
663 minerals to brockite and vanadatian brockite is relevant considering the proximity of the CHO to

664 shales of the Deadwood and Winnipeg Formations. The few other occurrences of brockite
665 throughout the BLAC also occur in close proximity to Paleozoic sedimentary rocks which seems
666 to point toward a lithologic control on REE+Th precipitation and mineral speciation (phosphates
667 rather than fluorocarbonates) as REE,Th-enriched fluids emanated outward toward the Paleozoic
668 section.

669 Recent studies (e.g., Migdisov et al. 2009) question the importance of fluoride complexes
670 as REE transport ligands in hydrothermal solutions, and suggest that chloride complexes may
671 play a vital role in REE transport, particularly in peralkaline granite and syenite complexes
672 (Williams-Jones et al. 2012). These conclusions are based on the stability of REE-fluoride
673 complexes at typical hydrothermal temperatures, high Cl^- concentrations and availability relative
674 to other ligands trapped in fluid inclusions (cf., Banks et al. 2004), and tendency toward
675 fluocerite [$(Ce,La,Nd)F_3$] saturation as a result of HF disassociation with increasing pH or
676 decreasing temperature. Unfortunately, fluorite at the CHO appears to be one of the few
677 generations of fluorite at Bear Lodge that does not contain fluid inclusions, preventing estimates
678 of chloride or phosphate concentrations in fluids which precipitated fluorite and possibly REE
679 phosphates. While $LREEF^{2+}$ species are more stable than $HREEF^{2+}$ species above 150°C,
680 $HREEF^{2+}$ species are more stable below this temperature (Williams-Jones et al. 2012). There is
681 some evidence that minerals at the CHO precipitated from low temperature fluids approaching
682 150°C; for example, the predominance of anatase over other TiO_2 polymorphs. In epithermal Au
683 systems the anatase to rutile transformation occurs at 150-200°C (Hendenquist et al. 2000), and
684 recent studies (Smith et al. 2009) confirm that crystallization of anatase requires low P-T,
685 aqueous conditions. The incorporation of H_2O or OH^- in phosphates and presence of

686 concentrically banded fluorite are further evidence for low temperature mineralization at the
687 CHO.

688 Studies of the solubility and aqueous complexation of Ti^{4+} and Nb^{5+} place further
689 constraints on fluid chemistry, as their solubility is relatively high in F- and P-rich solutions
690 known to transport REEs in alkaline igneous complexes (M□ller 1989; Morteani 1989 and
691 references therein). As hard Lewis acids, Ti^{4+} and Nb^{5+} are expected to form strong electrostatic
692 complexes with a hard Lewis base like F^-, even more so than Cl^-, a base of lesser hardness
693 (Pearson 1963, 1968; Rapp et al. 2010). Although Cl^- has recently received consideration as an
694 important REE transport ligand in hydrothermal fluids, Nb-chloride and Nb-sulfate complexes
695 are relatively weak and improbable transport ligands for Nb^{5+}, while Nb-fluoride complexes are
696 relatively strong (Babko and Shimadina 1959; Wood 2005). Highly acidic solutions with high
697 free-fluoride activities are thought to be more favorable for such complexes, although mixed Nb-
698 hydroxyfluoride complexes may permit Nb transport in more typical hydrothermal fluids (Wood
699 2005; Timofeev et al. 2015). These conclusions are also in agreement with studies of Ti^{4+}
700 solubility in F-rich solutions. Hydroxyfluoride complexes with Ti^{4+} were predominant in the
701 simple experimental solutions of Barsukova et al. (1979) and Purtov and Kotel'nikova (1993),
702 who found that Ti solubility increases with increasing m^0_{HF}/m^0_{HCl} and decreasing pH, although at
703 temperatures (400-700°C) much higher than those predicted for mineralization at the CHO.
704 More recent experiments exploring the solubility of rutile and Nb_2O_5 and mobility of Ti^{4+} and
705 Nb^{5+} (cf., Rapp et al. 2010; Tanis et al. 2015; Timofeev et al. 2015) are mostly performed
706 beyond the *T* and *P* range expected for the CHO, but reveal several relevant conclusions: 1)
707 rutile and Nb_2O_5 solubility and thus hydrothermal mobility of Ti and Nb is strongly dependent
708 on fluid chemistry, particularly halogen content, 2) Solubility is highest in F-rich solutions

relative to Cl-rich solutions, and increases with increasing *a*(F), 3) removal of F during precipitation of fluorite or fluorapatite will decrease Ti+Nb solubility and promote crystallization of Ti+Nb minerals, and 4) Ti+Nb should not be ubiquitously regarded as immobile, particularly in fluids with elevated halogen concentrations. The unusually high concentrations of Nb and Ti, and high Nb/Ti ratios of the CHO suggest that Paleozoic sediments are an improbable solitary source of HFSEs. Although anatase is a common weathering product of Fe-Ti oxides in heavy mineral sands and other sedimentary environments, high Nb/Ti ratios suggest either an alternative source or fractionating process (i.e., preferential transport of Nb in hydrothermal solution).

Acidic solutions with significant HF could explain the lack of quartz in rocks of the CHO, and presence of late recrystallized quartz in local breccias. Many of the secondary quartz-filled breccias and veins throughout the BLAC probably formed from solutions that dissolved SiO_2 from the Cambrian-Ordovician quartz sandstones or Archean granite, particularly the smoky quartz veins that transect the sandstones themselves. Our model for transport of HFSEs and HREEs in an acidic, low temperature, F(±P)–rich fluid hinges on the assumption that anatase, xenotime-(Y), brockite, and fluorite precipitated during Paleogene hydrothermal activity, and that no component crystallized during diagenesis of Cambrian-Ordovician sediments.

Implications

Fluid evolution in carbonatitic systems

This study demonstrates the extreme REE fractionation possible in carbonatite-derived fluids, and the possible role interaction with wall-rock lithologies may have on the precipitation of REE and Ti+Nb oxide minerals. Mineralization at the CHO is most consistent with formation

732 under low-temperature hydrothermal conditions, and while the CHO shares geochemical and
733 mineralogical similarities to placer-type Ti+REE occurrences or heavy mineral sands and
734 authigenic phosphate and Ti-oxide mineralization related to sedimentary diagenesis, a
735 carbonatitic source of REEs and HFSEs is more plausible. Although it seems improbable that a
736 fluid of such peculiar chemistry could travel more than 2 km through a variety of lithologies
737 without precipitating assemblages of similar hydrothermal minerals, an diagenetic origin for such
738 high concentrations of HREEs, Th, Ti, and Nb seems equally improbable, as the local
739 sedimentary units appear to be insufficient sources of these elements.
740 The unusual chemistry of the CHO is best explained by fractionation processes related to
741 carbonatites and carbo-hydrothermal fluids. LREEs are removed during crystallization of REE
742 carbonates and fluorocarbonates within the central carbonatite stockwork, leaving residual fluids
743 enriched in the most incompatible elements (HFSEs and HREEs). The abundance of REE
744 phosphates and REE fluorocarbonates in oxidized/altered carbonatite suggests increasing PO_4^{3-}
745 $/CO_3^{2-}$ and F^-/CO_3^{2-} ratios in late-stage fluids evolving toward a PO_4- and F-enriched and CO_3-
746 depleted composition consistent with CHO mineralogy. Studies addressing the solubility and
747 aqueous complexation of REEs, Ti, and Nb with Cl^-, F^-, CO_3^{2-}, SO_4^{2-}, and PO_4^{3-} suggest that F^- is
748 the mutual ligand with which REEs, Ti, and Nb all form relatively strong complexes, and that F-
749 rich hydrothermal fluids are capable of concentrating these elements. Major enrichment of Nb,
750 Y, F, Ti, Th, U, and to a lesser extent, Sc, Be, Sn, W, Se, and Li in the CHO is probably
751 analogous to the chemical evolution involving fractional crystallization and concentration of the
752 most incompatible elements similar to that proposed for NYF-type pegmatites.
753 The complexity of lithologic contacts near the CHO make it difficult to ascertain one
754 specific mechanism for REE deposition, but fluid interaction with shale, calcareous siltstone, and

sandstone probably played an important role. We suggest HFSEs and HREEs are transported in highly fractionated F-rich fluids of high ionic strength that originated from carbonatite intrusions or associated carbohydrothermal residua. With falling temperature and interaction with calcareous Paleozoic sedimentary rocks, HFSEs and HREEs precipitate as Nb-anatase, xenotime-(Y), brockite, and fluorite. The suspected lithologic control on REE precipitation makes the outer rim of Paleozoic sediments an attractive target for economic HFSE(+HREE) mineralization, and is a potentially useful model in similar alkaline-carbonatite complexes where late-stage HREE enrichment is observed.

REE phosphate mineralogy

The extraordinary HREE+Th concentrations of the CHO are consistent with the high modal abundance of xenotime-(Y) and brockite. Incorporation of Th, U, Ca, Si, and V in xenotime-(Y) may be more complicated than previously thought and a growing body of evidence suggests that substitution of these elements involves the incorporation of F^-, OH^- and/or H_2O. Compositional zoning in CHO xenotime-(Y) arises from cheralite-type substitution, where Th and Ca are introduced at the expense of REE+Y. Th/Ca-rich domains in xenotime-(Y) overgrowths deviate significantly from ideal stoichiometry, and are highly beam sensitive probably due to the presence of OH^- or H_2O. The suspected hydration of xenotime-(Y) may be related to co-precipitation with the H_2O-bearing phosphate, brockite, which is supported by the concomitant increase of Th and Ca within the most beam sensitive domains. Alternatively, H_2O or OH^- may have been introduced later by fluids that weakened and disrupted layers adjacent to the zircon substrate. Understanding actinide incorporation is important as xenotime receives considerable attention as a U-Pb geochronometer by in situ techniques. Further crystallographic and spectroscopic studies are required to understand actinide substitution and hydration in

778 xenotime-(Y) of the CHO, but it is clear that zones of variable actinide concentrations may have
779 a considerable effect on U-Pb ages determined by even the smallest diameter beam. Although
780 xenotime-(Y) outgrowths in local sandstones have a considerably different morphology
781 compared to CHO xenotime-(Y), their nearly indistinguishable compositions support a single
782 generation of xenotime-(Y) growth as fluids responsible for the CHO permeated the adjacent
783 sandstones. An earlier episode of xenotime-(Y) precipitation related to diagenesis of the
784 Cambrian-Ordovician sediments cannot be ruled out without in situ dating techniques.

785 Electron microprobe analyses show substantial VO_4^{3-} substitution for PO_4^{3-} in both
786 xenotime-(Y) and brockite, which further supports a sedimentary influence on REE precipitation,
787 as local clayshales contain the highest V concentrations of all Bear Lodge lithologies. Our
788 analyses of an undefined Ca-Th-Y-Ln phosphovanadate composition suggests a solid-solution
789 range may exist between brockite [$(Ca,Th,Ln)(PO_4)\cdot H_2O$] and a theoretical V-dominant end
790 member [$(Ca,Th,Ln)(VO_4)\cdot H_2O$], similar to the suspected miscibility between xenotime-(Y)
791 [YPO_4] and wakefieldite-(Y) [YVO_4].

792 **Acknowledgments**

793 The authors thank Washington State University's GeoAnalytical Laboratory and
794 technical staff. We especially thank Scott Boroughs for help with trace element analysis by LA-
795 ICP-MS, and Chris Fisher and Jeff Vervoort for help with U-Pb zircon analysis by LA-ICP-MS.
796 Anthony Mariano and Anthony Mariano Jr. are gratefully acknowledged for their guidance and
797 contributions. This research was funded primarily by Rare Element Resources Ltd. We thank
798 all RER personnel involved with this project. Helpful reviews by Olga Vasyukova and an
799 anonymous reviewer are greatly appreciated. We also extend our thanks to Associate Editor,
800 Peter Burns, for the editorial support.

References cited

Andersen, A.K., Cosca, M.A., and Larson, P.B. (2013a) Timing of carbonatite magmatism in the Bear Lodge alkaline complex, WY. Geological Society of America Abstracts with Programs, 45, 499.

Andersen, A.K., Larson, P.B., and Clark, J.G. (2013b) Rare earth element zonation and fractionation at the Bear Lodge REE Deposit, Wyoming. Geological Society of America, Rocky Mountain Section Meeting, Abstracts with Programs, 45, 42.

Andersen, A.K., Larson, P.B., and Rowe, M.C. (2013c) REE fractionation at the Bear Lodge REE+Au deposit, USA: Evidence from mineral chemistry. Mineralogical Magazine, Goldschmidt Abstracts, 77, 592.

Andrade, F.R.D., Möller, P., Lüders, V., Dulski, P., and Gilg, H.A. (1999) Hydrothermal rare earth elements mineralization in the Barra do Itapirapuã carbonatite, southern Brazil: behaviour of selected trace elements and stable isotopes (C, O). Chemical Geology, 155, 91–113.

Babko, A.K., and Shimadina, L.G. (1959) The stability of some fluoro metal complexes. Russian Journal of Inorganic Chemistry, 4, 482–485.

822 Banks, D.A., Yardley, B.W.D., Campbell. A.R., and Jarvis, K.E. (1994) REE composition of an
823 aqueous magmatic fluid: A fluid inclusion study from the Capitan Pluton, New Mexico,
824 U.S.A. Chemical Geology, 113, 259–272.
825
826 Barsukova, M.L., Kuznetsov, V.A., Dorofeyeva, V.A., and Khodakovskiy, I.L. (1979)
827 Measurement of the solubility of rutile TiO_2 in fluoride solutions at elevated
828 temperatures. Geochemistry International, 16, 41–49 (translated from Geokhimiya, 7,
829 1017–1027, 1979).
830 Bastos Neto, A.C., Pereira, V.P., Pires, A.C., Barbanson, L., and Chauvet, A. (2012) Fluorine-
831 rich xenotime from the world-class Madeira Nb-Ta-Sn deposit associated with the albite-
832 enriched granite at Pitinga, Amazonia, Brazil. Canadian Mineralogist, 50, 1453–1466.
833
834 Bau, M. (1996) Controls on the fractionation of isovalent trace elements in magmatic and
835 aqueous systems: evidence from Y/Ho, Zr/Hf, and lanthanide tetrad effect. Contributions
836 to Mineralogy and Petrology, 123, 323–333.
837
838 Bau, M. (1999) Scavenging of dissolved yttrium and rare earths by precipitating iron
839 oxyhydroxide: experimental evidence for Ce oxidation, Y–Ho fractionation, and
840 lanthanide tetrad effect. Geochimica et Cosmochimica Acta, 63, 67–77.
841
842 Bau, M., and Dulski P. (1995) Comparative study of yttrium and rare-earth element behaviors in
843 fluorine-rich hydrothermal fluids. Contributions to Mineralogy and Petrology, 119, 213–
844 223.

Bau, M., and Dulski, P., (1999) Comparing yttrium and rare earths in hydrothermal fluids from the Mid-Atlantic Ridge: implications for Y and REE behavior during near vent mixing and for the Y/Ho ratio of Proterozoic seawater. Chemical Geology, 155, 77–79.

Bau, M., Romer R. L., Lüders V., and Dulski P. (2003) Tracing element sources of hydrothermal mineral deposits: REE and Y distribution and Sr–Nd–Pb isotopes in fluorite from MVT deposits in the Pennine Orefield, England. Mineralium Deposita, 38, 992–1008.

Berger, A., Gnos, E., Janots, E., Fernandez, A., and Giese, J. (2008) Formation and composition of rhabdophane, bastnäsite and hydrated thorium minerals during alteration: Implications for geochronology and low-temperature processes. Chemical Geology, 254, 238–248.

Bickford, M.E., Collerson, K.D., Lewry, J.F., van Schmus, W.R., and Chiarenzelli, J.R. (1990) Proterozoic collisional tectonism in the Trans-Hudson orogen, Saskatchewan. Geology, 18, 14–18.

Bühn, B. (2008) The role of the volatile phase for REE and Y fractionation in low-silica carbonate magmas: implications from natural carbonatites, Namibia. Mineralogy and Petrology, 92, 453–470.

Byrne, R.H., and Kim, K.H. (1993) Rare earth precipitation and coprecipitation behavior. The limiting role of $PO4^{3-}$ on dissolved rare earth concentrations in seawater. Geochimica et Cosmochimica Acta, 57, 519–526.

Byrne, R.H., and Li, B. (1995) Comparative complexation behavior of the rare earths. Geochimica et Cosmochimica Acta, 59, 4575–4589.

Carlson, R.W., and Irving, A.J. (1994) Depletion and enrichment history of subcontinental lithospheric mantle: an Os, Sr, Nd, Pb isotopic study of ultramafic xenoliths from the northwestern Wyoming Craton. Earth and Planetary Science Letters, 126, 457–472.

Cetiner, Z.S. (2003) Experimental investigation of the solubility of the REE phosphate minerals monazite/xenotime and chloride complexation in hydrothermal solutions at 23°C, 50°C, and 150°C and saturated water vapor pressure,154 p. Ph.D. thesis, University of Idaho, Moscow, U.S.A.

Chakhmouradian, A.R., and Mitchell, R.H. (1998) Lueshite, pyrochlore and monazite-(Ce) from apatite–dolomite carbonatite, Lesnaya Varaka complex, Kola Peninsula, Russia. Mineralogical Magazine, 62, 769–782.

Chamberlain, K.R., Frost, C.D., and Frost, B.R. (2003) Early Archean to Mesoproterozoic evolution of the Wyoming Province: Archean origins to modern lithospheric architecture. Canadian Journal of Earth Sciences, 40, 1357–1374.

Chang, Z., Vervoort, J.D., McClelland, W.C., and Knaack, C. (2006) U-Pb dating of zircon by LA-ICP-MS. Geochemistry, Geophysics, Geosystems, 7, 1–14.

Corfu, F., Hanchar, J.M., Hoskin, P.W.O., and Kinny, P. (2003) Atlas of zircon textures. In J.M. Hanchar and P.W.O. Hoskin, Eds., Zircon, 53, p. 469–500. Reviews in Mineralogy and Geochemistry, Mineralogical Society of America, Chantilly, Virginia.

Cox, D.M., Frost, C.D., and Chamberlain, K.R. (2000) 2.01 Ga Kennedy dike swarm, southeastern Wyoming: record of a rifted margin along the southern Wyoming province. Rocky Mountain Geology, 35, 7–30.

Dahl, P.S., and Frei, R. (1998) Single-phase dating of coexisting garnet and staurolite in the Black Hills collisional orogen (South Dakota), with implications for Early Proterozoic tectonism. Geology, 26, 111–114.

Dahl, P.S., Holm, D.K., Gardner, E.T., Hubacher, F.A., and Foland, K.A. (1999) New constraints on the timing of Early Proterozoic tectonism in the Black Hills (South Dakota), with implications for the docking of the Wyoming province with Laurentia. Geological Society of America Bulletin, 111, 1335–1349.

Dahl, P.S., Hamilton, M.A., Jercinovic, M.J., Terry, M.P., Williams, M.L., and Frei, R. (2005a) Comparative isotopic and chemical geochronometry of monazite, with implications for

U-Th-Pb dating by electron microprobe: An example from metamorphic rocks of the eastern Wyoming craton (U.S.A.). American Mineralogist, 90, 619–638.

Dahl, P.S., Terry, M.P., Jercinovic, M.J., Williams, M.L., Hamilton, M.A., Foland, K.A., Clement, S.M., and Friberg, L.M. (2005b) Electron probe (Ultrachron) microchronometry of metamorphic monazite: unraveling the timing of polyphase thermotectonism in the easternmost Wyoming Craton (Black Hills, South Dakota). American Mineralogist, 90, 1712–1728.

Dahlberg, P.S., Noble, A.C., Pickarts, J.T., Rose, W.L., Jaacks, J.A. (2014) Technical Report on the Reserves and Development of the Bul Hill Mine, Wyoming. Rare Element Resources, Ltd. Bear Lodge Project Canadian NI 43-101 Pre-Feasibility Technical Report, Oct. 9, 2014.

Donovan, J.J., Synder, D.A., and Rivers, M.L. (1993) An improved intereference correction for trace element analysis. Microbeam Analysis, 2, 23–28.

Donovan, J.J., Kremser, D., and Fournelle, J.H. (2007) Probe for Windows User's Guide and Reference, Enterprise Edition., 355 p. Probe Software, Inc., Eugene, Oregon.

Duke, G.I. (2005) Geochemistry and Geochronology of Paleocene-Eocene Alkalic Igneous Rocks, Northern Black Hills, South Dakota and Wyoming, 291 p. Ph.D. thesis, South Dakota School of Mines and Technology, Rapid City, U.S.A.

Firsching, F.H., and Brune, S.N. (1991) Solubility products of the trivalent rare-earth phosphates. Journal of Chemical and Engineering Data, 36, 93–95.

Fisher, F.G., and Meyrowitz, R. (1962) Brockite, a new calcium thorium phosphate from the Wet Mountains, Colorado. American Mineralogist, 47, 1346–1355.

Force, E.R. (1991) Geology of Titanium-Mineral Deposits. Geological Society of America Special Paper, 259, 112 p.

Förster, H.-J. (1998a) The chemical composition of REE–Y–Th–U-rich accessory minerals in peraluminous granites of the Erzgebirge–Fichtelgebirge region, Germany. I. The monazite-(Ce)–brabantite solid-solution series. American Mineralogist, 83, 259–272.

Förster, H.-J. (1998b) The chemical composition of REE–Y–Th–U-rich accessory minerals in peraluminous granites of the Erzgebirge–Fichtelgebirge region, Germany. II. Xenotime. American Mineralogist, 83, 1302–1315.

Förster, H.-J. (2006) Composition and origin of intermediate solid solutions in the system thorite−xenotime−zircon−coffinite. Lithos, 88, 35–55.

Frost, C.D., and Fanning, C.M. (2006) Archean geochronological framework of the Bighorn Mountains, Wyoming. Canadian Journal of Earth Sciences, 43, 1399–1418.

Göb, S., Wenzel, T., Bau, M., Jacob, D.E., Loges, A., and Markl, G. (2011) The redistribution of rare-earth elements in secondary minerals of hydrothermal veins, Schwarzwald, SW Germany. Canadian Mineralogist, 49, 1305–1333.

Goldstein, J., Newbury, D., Echlin, P., Joy, D., Fiori, D., and Lifshin, E. (1984) Scanning Electron Microscopy and X-ray Microanalysis, 690 p. Plenum, New York.

Gramaccioli, C.M., and Segalstad, T.V. (1978) A uranium- and thorium-rich monazite from a south-alpine pegmatite at Piona, Italy. American Mineralogist, 63, 757–761.

Harlov, D.E., and Wirth, R. (2012) Experimental incorporation of Th into xenotime at middle to lower crustal *P-T* utilizing alkali-bearing fluids. American Mineralogist, 97, 641–652.

Hay, D.C., Dempster, T.J., Lee, M.R., and Brown, D.J. (2010) Anatomy of a low temperature zircon outgrowth. Contributions to Mineralogy and Petrology, 159, 81–92.

Hedenquist, J.W., Arribas, A., and Eliseo, G.-U. (2000) Exploration for Epithermal Gold Deposits. In S.G. Hagemann and P.E. Brown, Eds., Gold in 2000, 13, 245–277. Society of Economic Geologists Reviews, Littleton, CO.

Hetherington C.J., and Harlov, D.E. (2008) Metasomatic thorite and uraninite inclusions in xenotime and monazite from granitic pegmatites, Hidra anorthosite massif, southwestern Norway: mechanics and fluid chemistry. American Mineralogist, 93, 806–820.

Hetherington, C.J., Jercinovic, M.J., Williams, M.L., and Mahan, K. (2008) Understanding geologic processes with xenotime: Composition, chronology, and a protocal for electron probe microanalysis. Chemical Geology, 254, 133–147.

Ixer, R.A., Turner, P., and Waugh, B. (1979) Authigenic iron and titanium oxides in Triassic red beds: (St. Bees Sandstone), Cumbria, Northern England. Geological Journal, 14, 179–192.

Ixer, R.A., and Vaughan, D.J. (1982) The primary ore mineralogy of the Alderley Edge deposit, Cheshire. Mineralogical Magazine, 46, 485–492.

Johan, Z., and Johan, V. (2004) Accessory minerals of the Cínovec (Zinnwald) granite cupola, Czech Republic: indicators of petrogenetic evolution. Mineralogy and Petrology, 83, 113–150.

Jackson, S.E., Longerich, H.P., Dunning, G.R., Fryer, B.J. (1992) The application of laser-ablation microprobe – inductively coupled plasma – mass spectrometry (LAM–ICP–MS) to in situ trace-element determinations in minerals. Canadian Mineralogist, 30, 1049–1064.

Jonasson, R.G., Bancroft, G.M., and Nesbitt, H.W. (1985) Solubilities of some hydrous REE phosphates with implications for diagenesis and seawater concentrations. Geochimica et Cosmochimica Acta, 49, 2133–2139.

Kolitsch, U., and Holtstam, D. (2004) Crystal chemistry of $REEXO_4$ compounds (X=P,As,V). II. Review of $REEXO_4$ compounds and their stability fields. European Journal of Mineralogy, 16, 117–126.

Kositcin, N., McNaughton, N.J., Griffin, B.J., Fletcher, I.R., Groves, D.I. and Rasmussen, B. (2003) Textural and geochemical discrimination between xenotime of different origin in the Archaean Witwatersrand Basin, South Africa. Geochimica et Cosmochimica Acta, 67, 709–731.

Krenn, E., and Finger, F. (2007) Formation of monazite and rhabdophane at the expense of allanite during Alpine low temperature retrogression of metapelitic basement rocks from Crete, Greece: Microprobe data and geochronological implications. Lithos, 95, 130–147.

Lee, J.H., and Byrne, R.H. (1992) Examination of comparative rare earth element complexation behavior using linear free-energy relationships. Geochimica et Cosmochimica Acta, 56, 1127–1137.

Linnen, R.L., Samson, I.M., Williams-Jones, A.E., and Chakhmouradian, A.R. (2014)

Geochemistry of the rare-earth elements, Nb, Ta, Hf, and Zr deposits. In H.D. Holland and K.K. Turekian, Eds., Treatise on Geochemistry, Second Edition. Geochemistry of Mineral Deposits, 13, p. 543–568. Elsevier, Oxford.

Linthout, K. (2007) Tripartite division of the system $2REEPO_4$–$CaTh(PO_4)_2$–$2ThSiO_4$, discreditation of brabantite, and recognition of cheralite as the name for members dominated by $CaTh(PO_4)_2$. Canadian Mineralogist, 45, 503–508.

Liu, X., and Byrne, R.H. (1997) Rare earth and yttrium phosphate solubilities in aqueous solution. Geochimica et Cosmochimica Acta, 61, 1625–1633.

Loges, A., Wagner, T., Barth, M., Bau, M., Göb, S., and Markl, G. (2012) Negative Ce anomalies in Mn oxides: the role of Ce^{4+} mobility during water-mineral interaction. Geochimica et Cosmochimica Acta, 86, 296–317.

Lumpkin, G.R, and Chakoumakos, B.C. (1986) Thorite group minerals from the Harding mine, Taos County, New Mexico (abs.). Geological Association of Canada-Mineralogical Association of Canada Joint Annual Meeting, 11, 96–97.

Lumpkin, G.R., and Chakoumakos, B.C. (1988) Chemistry and radiation effects of thorite-group minerals from the Harding pegmatite, Taos County, New Mexico. American Mineralogist, 73, 1405–1419.

Luo, Y-R., and Byrne, R.H. (2001) Yttrium and rare earth element complexation by chloride ions at 25°C. Journal of Solution Chemistry, 30, 837–845.

Mariano, A.N. (1981) Rare earth mineralization in the Bear Lodge carbonatite complex, Crook County, Wyoming. Confidential Report to Molycorp Inc., 52 p.

Mariano, A.N. (1989a) Economic geology of rare earth elements. In B.R. Lipin and G.A. McKay Eds., Geochemistry and Mineralogy of Rare Earth Elements, 21, p 309–337. Reviews in Mineralogy and Geochemistry. Mineralogical Society of America, Chantilly, Virginia.

Mariano, A.N. (1989b) Nature of economic mineralization in carbonatites and related rocks. In K. Bell, Ed., Carbonatites—Genesis and Evolution, p. 149–176. Unwin Hyman, London.

Mariano, A.N. (2009) Carbocernaite, a major REE mineral in the Bear Lodge carbonatite rock units. Confidential Report to Rare Element Resources Ltd., 11 p.

Mariano, A.N., and Mitchell, R.M. (2009) Large-scale development of supergene anatase-rich soils on carbonatite-associated pyroxenites in Brazil (abs.). In S.R. Titley, Ed., Supergene Environments, Processes, and Products. Society of Economic Geologists, Special Publication 14, 149.

McDonough, W.F., and Sun, S.-s. (1995) The composition of the Earth. Chemical Geology, 120, 223–253.

McDowell, F.W. (1971) K-Ar ages of igneous rocks from the western United States: Isochron/West, 2, 1–16.

Migdisov A. A., Williams-Jones A. E., and Wagner T. (2009) An experimental study of the solubility and speciation of the Rare Earth Elements (III) in fluoride- and chloride-bearing aqueous solutions at temperatures up to 300°C. Geochimica et Cosmochimica Acta, 73, 7087–7109.

M□ller, P. (1989) REE(Y), Nb, and Ta enrichment in pegmatites and carbonatite-alkalic rock complexes. In P. Möller, P. Černý, and F. Saupé, Eds., Lanthanides, Tantalum, and Niobium. Proceedings of a workshop in Berlin, November 1986, p. 103–144. Special Publication No. 7 of the Society for Geology Applied to Mineral Deposits, Springer-Verlag, Berlin.

Moore, M., Chakhmouradian, A.R., Mariano, A.N., and Sidhu, R. (2014) Evolution of rare-earth mineralization in the Bear Lodge carbonatite, Wyoming: Mineralogical and isotopic evidence. Ore Geology Reviews, 64, 499–521.

Morad, S., and Aldahan, A.A. (1982) Authigenesis of titanium minerals in two Proterozoic sedimentary rocks from southern and central Sweden. Journal of Sedimentary Geology, 52, 1295–1305.

Morteani, G. (1989) Prospection for niobium-rich alkaline rocks. In P. Möller, P. Černý, and F. Saupé, Eds., Lanthanides, Tantalum, and Niobium. Proceedings of a workshop in Berlin, November 1986, p. 311–320. Special Publication No. 7 of the Society for Geology Applied to Mineral Deposits, Springer-Verlag, Berlin.

Mueller, P.A., and Frost, C.D. (2006) The Wyoming Province: a distinctive Archean craton in Laurentian North America. Canadian Journal of Earth Sciences, 43, 1391–1397.

Mueller, P.A., Heatherington, A.L., Kelly, D.M., Wooden, J.L., and Mogk, D.W. (2002) Paleoproterozoic crust within the Great Falls tectonic zone: implications for the assembly of southern Laurentia. Geology, 30, 127–130.

Olin, P.H., and Wolff, J.A. (2010) Rare earth and high field strength element partitioning between iron-rich clinopyroxenes and felsic liquids. Contributions to Mineralogy and Petrology, 160, 761–775.

Olin, P.H., and Wolff, J.A. (2012) Partitioning of rare earth and high field strength elements between titanite and phonolitic liquid. Lithos, 128, 46–54.

Pearson, R.G. (1963) Hard and soft acids and bases. Journal of the American Chemical Society, 85, 3533–3539.

Pearson, R.G. (1968) Hard and soft acids and bases HSAB 1. Fundamental principles. Journal of

Chemical Education, 45, 581–587.

Pointer, C.M., Ashworth, J.R., and Ixer, R.A. (1988) The zircon–thorite mineral group in metasomatized granite, Ririwai, Nigeria 1. Geochemistry and metastable solid solution of thorite and coffinite. Mineralogy and Petrology, 38, 245–262.

Purtov, V.K., and Kotel'nikova, A.L. (1993) Solubility of titanium in chloride and fluoride hydrothermal solutions. International Geology Review, 35, 279–287.

Pyle, J., Spear, F., and Wark, D.A. (2002) Electron Microprobe analysis of REE in apatite, monazite and xenotime: protocols and pitfalls. In M.L. Kohn, J. Rakovan, J.M. Hughes, Eds., Phosphates: Geochemical, Geobiological, and Materials Importance, 48, p. 337–362. Reviews in Mineralogy and Geochemistry, Mineralogical Society of America, Chantilly, Virginia.

Rapp, J.F., Klemme, S., Butler, I.B., and Harley, S.L. (2010) Extremely high solubility of rutile in chloride and fluoride-bearing metamorphic fluids: An experimental investigation. Geology, 38, 323–326.

Rasmussen, B. (1996) Early-diagenetic REE-phosphate minerals (florencite, gorceixite, crandallite, and xenotime) in marine sandstones: A major sink for oceanic phosphorus. American Journal of Science, 296, 601–632.

Rasmussen, B. (2005) Radiometric dating of sedimentary rocks: the application of diagenetic xenotime geochronology. Earth-Science Reviews, 68, 197–243.

Rasmussen, B., and Glover, J.E. (1994) Diagenesis of low-mobility elements (Ti, REE and Th) and solid bitumen envelopes in Permian Kennedy Group sandstone, Western Australia. Journal of Sedimentary Research, 64, 572–583.

Rasmussen, B., and Glover, J.E. (1996) Fluid evolution interpreted from diagenetic assemblages and salinity data in Permo –Triassic sandstone, northern Perth Basin, Western Australia. Journal of Sedimentary Research, 66, 492–500.

Roder, P.L. (1985) Electron-microprobe analysis of minerals for rare-earth elements: Use of calculated peak-overlap corrections. Canadian Mineralogist, 23, 263–271.

Rudnick, R.L., Ireland, T.R., Gehrels, G., Irving, A.J., Chelsey, J.T., and Hanchar, J.M. (1999) Dating mantle metasomatism: U-Pb geochronology of zircons in cratonic mantle xenoliths from Montana and Tanzania. In J.J. Gurney, J.L. Gurney, M.D. Pascoe, and S.H. Richardson, Eds., Proceedings of the VIIth International Kimberlite Conference, 2, p. 728–735.

Salvi, S., and Williams-Jones, A. (1996) The role of hydrothermal processes in concentrating high-field strength elements in the Strange Lake peralkaline complex, northeastern Canada. Geochimica et Cosmochimica Acta, 60, 1917–1932.

Salvi, S., and Williams-Jones, A. (2005) Alkaline granite-syenite deposits. In R.L. Linnen and I.M. Samson, Eds., Rare-Element Geochemistry and Mineral Deposits. Geological Association of Canada, Short Course Notes, 17, 315–341.

Schijf, J., and Byrne, R.H. (1999) Determination of stability constants for the mono- and difluoro-complexes of Y and the REE, using a cation-exchange resin and ICP-MS. Polyhedron, 18, 2839–2844.

Selleck, B.W. (2008) Stratigraphy, sedimentology and diagenesis of the Potsdam formation, Southern Lake Champlain Valley, New York. New York State Geological Association, Fieldtrip Guidebook, 80th Annual Meeting, 1–13.

Selleck, B.W., Williams, M., and Jercinovic, M. (2008) In situ U-Th-Pb microprobe dating of authigenic monazite and xenotime in the Potsdam sandstone, eastern New York: A new approach to dating hydrothermal fluid flow and dolomitization. Eastern Section AAPG Abstracts, 2008.

Shoji, H., and Akai, J. (1994) Brockite from Ishikawa, Fukushima Prefecture, Japan. Science Reports of Niigata University, Series E, 9, 89–96.

Sims, P.K., and Peterman, Z.E. (1986) Early Proterozoic Central Plains orogen: A major buried structure in the north-central United States. Geology, 14, 488–491.

Smith, M.P., Henderson, P., and Campbell, L.S. (2000) Fractionation of the REE during hydrothermal processes: Constraints from the Bayan Obo Fe-REE-Nb deposit, Inner Mongolia, China. Geochimica et Cosmochimica Acta, 64, 3141–3160.

Smith, S.J., Stevens, R., Liu, S., Li, G., Navrotsky, A., Boerio-Goates, J., and Woodfield, B.F. (2009) Heat capacities and thermodynamic functions of TiO_2 anatase and rutile: Analysis of phase stability. American Mineralogist, 94, 236–243.

Staatz, M.H. (1983) Geology and Description of Thorium and Rare-Earth Deposits in the Southern Bear Lodge Mountains, Northeastern Wyoming, 52 p. U.S. Geological Survey Professional Paper 1049-D.

Tanis, E.A., Simon, A., Tschauner, O., Chow, P., Xiao, Y., Burnley, P., Cline, C.J. II, Hanchar, J.M., Pettke, T., Shen, G., and Zhao, Y. (2015) The mobility of Nb in rutile-saturated NaCl- and NaF-bearing aqueous fluids from 1–6.5 GPa and 300–800°C. American Mineralogist, 100, 1600–1609.

Taylor, S.R., and McLennan, S.M. (1985) The Continental Crust: Its Composition and Evolution, 312 p. Blackwell, Oxford.

Timofeev, A., Migdisov, A.A., and Williams-Jones, A.E. (2015) An experimental study of the solubility and speciation of niobium in fluoride-bearing aqueous solutions at elevated temperature. Geochimica et Cosmochimica Acta, 158, 103–111.

Liu, T., Wang, G., and Gong, J. (1987) Study on brockite first found in Bayan Obo, China. Acta Mineralogica Sinica 7 (2), 177–182 (in Chinese).

Vallini, D., Rasmussen, B., Krapez, B., Fletcher, I.R., and McNaughton, N.J. (2002) Obtaining diagenetic ages from metamorphosed sedimentary rocks: U–Pb dating of unusually coarse xenotime cement in phosphatic sandstone. Geology, 30, 1083–1086.

Vallini, D., Rasmussen, B., Krapez, B., Fletcher, I.R., and McNaughton, N.J. (2005) Microtextures, geochemistry and geochronology of authigenic xenotime: constraining the cementation history of a Palaeoproterozoic metasedimentary sequence. Sedimentology, 52, 101–122.

van Emden, B., Thornber, M.R., Graham, J., and Lincoln, F.J. (1997) The incorporation of actinides in monazite and xenotime from placer deposits in western Australia. Canadian Mineralogist, 35, 95–104.

Van Wambeke, L. (1977) The Karonge rare earth deposits, Republic of Burundi: New mineralogical–geochemical data and origin of the mineralization. Mineralium Deposita, 12, 373–380.

Vogl, J.J., Foster, D.A., Mueller, P.A., Mogk, D.W., and Wooden, J.L. (2002) Age and character of Precambrian basement in the Little Belt Mountains, Montana; implications for the role of the Great Falls tectonic zone in the Paleoproterozoic assembly of North America. Geological Society of America Abstracts with Programs, 34.

Wall, F., Niku-Paavola, V.N., Storey, C., Muller, A., and Jefferies, T. (2008) Xenotime-(Y) from carbonatite dykes at Lofdal, Namibia: unusually low LREE/HREE ratio in carbonatite, and the first dating of xenotime overgrowths on zircon. Canadian Mineralogist, 46, 861–877.

Walter, A.-V., Flicoteaux, R., Parron, C., Loubet, M., and Nahon, D. (1995) Rare-earth elements and isotopes (Sr, Nd, O, C) in minerals from the Juquiá carbonatite (Brazil): tracers of a multistage evolution. Chemical Geology, 120, 27–44.

Watt, G.R. (1995) High-thorium monazite-(Ce) formed during disequilibrium melting of metapelites under granulite-facies conditions. Mineralogical Magazine, 59, 735–743.

Williams, C.T. (1996) Analysis of rare earth minerals. In A.P. Jones, F. Wall, C.T. Williams, Eds., Rare Earth Minerals: Chemistry, Origin and Ore Deposits. Mineralogical Society Series, 7, 327–348.

Williams-Jones A. E., Migdisov A. A., and Samson I. M. (2012) Hydrothermal mobilisation of the Rare Earth Elements – a Tale of "Ceria" and "Yttria". Elements, 8, 355–360.

Wood, S. A. (1990a) The aqueous geochemistry of the rare-earth elements [REE] and yttrium. 1. Review of available low temperature data for inorganic complexes and the inorganic REE speciation of natural waters. Chemical Geology, 82, 159–186.

Wood, S. A. (1990b) The aqueous geochemistry of the rare-earth elements and yttrium. 2. Theoretical predictions of speciation in hydrothermal solutions to 350°C at saturation water vapor pressure. Chemical Geology, 88, 99–125.

Wood, S.A. (2003) The geochemistry of rare earth elements and yttrium in geothermal waters. In S.F. Simmons and I. Graham, Eds., Volcanic, Geothermal and Ore-forming Fluids: Rulers and Witnesses of Processes within the Earth. Special Publication, 10, p. 133–158. Society of Economic Geologists, Littleton, CO.

Wood, S.A. (2005) The Aqueous Geochemistry of Zirconium, Hafnium, Niobium and Tantalum. In R. Linnen and I. Samson, Eds., Rare-Element Geochemistry and Mineral Deposits. Geological Association of Canada Short Course Notes, 17, 217–251.

Figure Captions

Figure 1. Simplified geologic map of the Bear Lodge alkaline complex (BLAC) showing position of the Cole HFSE(+HREE) Occurrence (CHO) relative to central REE-rich carbonatite intrusions. Inset map (**lower left**) shows position of the BLAC in the northern Black Hills region

1276 near the South Dakota-Wyoming border. Dashed black circle encompasses a majority of REE
1277 mineralization hosted by carbonatite veins and dikes and their oxidized equivalents. The CHO
1278 occurs near the first outward occurrence of Paleozoic sedimentary rocks.
1279
1280 **Figure 2.** BSE images of minerals and textures from the Cole HFSE(+HREE) Occurrence. (**a**)
1281 Typical morphology of anatase in the CHO. (**b**) Typical mineralogy and texture of CHO rocks
1282 including zircon (zrn) with xenotime-(Y) (xtm) outgrowths, anatase (ant) coating corroded K-
1283 feldspar (Kfs), brockite (bro), and interstitial fluorite (fl). (**c**) Nb-zoned anatase on K-feldspar.
1284 (**d**) Anatase druses on fragmented K-feldspar and late void-filling botryoidal fluorite. (**e**) Nb-
1285 zoned anatase nucleating from zircon with zoned xenotime-(Y) outgrowths. (**f**) Cluster of
1286 hexagonal brockite crystals. (**g**) Void-filling xenotime-(Y) (gray) and brockite (white). Note the
1287 intergrown texture of xenotime-(Y) and brockite and innermost crust which is predominately
1288 brockite. (**h,i**) Sections through striated/banded dipyramidal xenotime-(Y) overgrowths on zircon
1289 substrate. (**j,k**) Serrated and bulbous diagenetic xenotime-(Y) outgrowths on zircon in Cambrian-
1290 Ordovician sandstones adjacent to the CHO. (**l**) Secondary electron image of triangular voids left
1291 when xenotime-(Y) outgrowths are dislodged during thin section sample preparation.
1292
1293 **Figure 3.** (**a**) Whole rocks trace element concentrations of CHO rocks normalized to average
1294 unoxidized Bear Lodge carbonatite. (**b**) Chondrite normalized trace element pattern of CHO
1295 rocks compared with potential source rocks at Bear Lodge (Appendix Table 2). Chondrite values
1296 of McDonough and Sun (1995).
1297

1298 **Figure 4.** Chondrite normalized REE pattern of brockite, and an exsolved Ca-Th-Y-REE
1299 phosphovanadate phase from the CHO compared with brockite form the type locality. The Y
1300 depletion relative to adjacent REEs of similar charge and radius (Dy and Ho) in CHO brockite
1301 probably results from co-crystallization with xenotime-(Y) and/or fluorite. However, this trend
1302 is also observed in brockite from the Wet Mountains, CO (Fisher and Meyrowitz, 1962) which
1303 may suggest a crystal structural control rather than co-crystallization of an Y-dominant phase like
1304 xenotime-(Y). Chondrite values of Taylor and McLennan (1985).
1305
1306 **Figure 5.** Possible substitution vectors in xenotime-(Y) and brockite from the CHO. Filled
1307 circles: banded xenotime-(Y) overgrowths, open circles: disseminated xenotime, squares:
1308 sandstone-hosted xenotime-(Y) outgrowths, filled rhombs: brockite, open rhombs: Ca-Th-Y-REE
1309 phosphovanadate. TREO = total rare earth oxide. Plots include additional data available in
1310 Appendix Tables 3 and 4. Note: In Figs. 5b and 5c, strong correlation is observed only for
1311 xenotime-(Y) overgrowths, not disseminated xenotime.
1312
1313 **Figure 6.** BSE images of xenotime-(Y) overgrowths and V-rich exsolution in brockite from the
1314 Cole HFSE(+HREE) Occurrence. (**a**) Bright white patches are portions of brockite where
1315 significant VO_4 has substituted for PO_4. (**b**) banded xenotime-(Y) outgrowth showing alternating
1316 zones of variable hydration. Solid white circles show spots with little degradation under electron
1317 beam, while darker Th/Ca-rich hydrated zones show significant damage under the same beam
1318 conditions (20 kV, 15 nA). (**c**) Arrow points toward remobilized, hydrated layers within
1319 xenotime-(Y) outgrowth. (**d**) Disaggregated, recrystallized xenotime-(Y) adjacent to zircon

1320 substrate. (**e**) Dipyramidal xenotime-(Y) overgrowth with anatase (arrows) along boundary
1321 between irregular, disaggregated xenotime-(Y) and uniformly banded xenotime-(Y).
1322
1323 **Figure 7.** Chondrite normalized REE patterns for xenotime-(Y) and brockite. Shaded region
1324 includes banded xenotime-(Y) overgrowths including low H_2O domains. Xenotime-(Y)
1325 outgrowths from adjacent sandstone (white boxes) have similar REE distributions to xenotime-
1326 (Y) from the CHO. Brockite from the CHO contains slightly higher concentrations of LREEs.
1327 Xenotime-(Y) and brockite exhibit opposing trends, particularly between Gd and Ho, as a result
1328 of co-crystallization. Chondrite values of Taylor and McLennan (1985).
1329
1330 **Figure 8.** Chondrite normalized REE patterns for fluorite hosted by different lithologies
1331 throughout the BLAC. Data were calculated using Ca as an internal standard at concentrations
1332 previously determined by EPMA. Fluorite at the CHO is HREE-dominant, while fluorite hosted
1333 by all other lithologies throughout the BLAC are LREE-dominant. Sample numbers correspond
1334 to descriptions and data in Table 3. Sample 12BL09, an additional fluorite vein near the CHO, is
1335 similarly enriched in HREEs. Chondrite values of Taylor and McLennan (1985).
1336
1337 **Figure 9.** Soil geochemistry map of the BLAC showing circular Y-anomaly which corresponds
1338 with Mississippian Pahasapa (Madison) limestone (figure courtesy of Jeffrey Jaacks,
1339 Geochemical Applications International, Inc.). Elevated Y concentrations are probably a
1340 product of the high abundance of fluorite which crystallized as outward emanating F-rich fluids
1341 interacted with Ca-rich lithologies. Some karst cavities within the Pahasapa (Madison) limestone
1342 are partially filled with fluorite.

1343

1344

1345

This is a preprint, the final version is subject to change, of the American Mineralogist (MSA)
Cite as Authors (Year) Title. American Mineralogist, in press.
(DOI will not work until issue is live.) DOI: http://dx.doi.org/10.2138/am-2016-5532

Table 1a. Representative analyses of brockite

	71-bro-1	71-bro-2	71-bro-4	71-bro-5	71-bro-10	71-bro-10b	71-bro-11	23-bro-1	23-bro-3	23-bro-4	23-bro-9	23-bro-9b
SiO_2	0.21	0.16	0.20	0.16	0.08	0.22	0.24	0.16	0.14	0.17	0.13	0.20
P_2O_5	27.27	26.25	26.88	26.78	27.08	26.18	26.91	26.01	27.00	25.71	27.20	26.30
SO_3	0.18	0.96	0.32	0.82	0.43	0.67	0.32	1.24	0.65	0.68	0.67	1.68
V_2O_5	0.11	- - -	0.08	- - -	0.08	0.15	0.10	0.08	0.11	0.60	0.36	0.04
CaO	11.80	13.55	13.62	14.64	9.79	11.52	11.11	14.59	14.40	14.49	13.86	15.91
FeO	0.66	0.22	0.68	0.41	0.16	0.86	0.36	0.26	0.16	0.07	0.10	0.28
SrO	1.11	1.24	0.92	1.09	1.65	1.17	1.03	1.43	1.12	1.12	1.08	1.40
BaO	1.14	0.82	0.99	0.88	0.82	0.96	1.00	0.77	0.88	0.58	0.74	0.68
Y_2O_3	4.81	3.77	4.86	3.88	5.24	4.28	4.95	3.16	3.84	3.30	3.86	3.23
La_2O_3	0.32	0.15	0.39	0.26	0.25	0.23	0.52	0.31	0.31	0.29	0.33	0.25
Ce_2O_3	0.50	0.26	0.37	0.37	0.50	0.41	0.66	0.58	0.45	0.58	0.47	0.52
Pr_2O_3	0.06	- - -	0.10	0.06	0.07	- - -	0.08	- - -	0.06	0.12	- - -	- - -
Nd_2O_3	0.35	0.19	0.38	0.27	0.25	0.26	0.37	0.36	0.26	0.34	0.29	0.25
Sm_2O_3	0.65	0.35	0.58	0.39	0.60	0.38	0.40	0.46	0.38	0.39	0.46	0.30
Eu_2O_3	0.40	0.25	0.36	0.22	0.40	0.28	0.28	0.33	0.25	0.27	0.31	0.28
Gd_2O_3	1.59	1.02	1.59	1.18	1.57	1.23	1.28	1.24	1.12	1.16	1.18	1.05
Tb_2O_3	0.32	0.22	0.34	0.27	0.27	0.20	0.28	0.19	0.23	0.20	0.22	0.21
Dy_2O_3	1.61	1.34	1.78	1.37	1.52	1.42	1.56	1.26	1.36	1.11	1.27	1.28
Ho_2O_3	0.19	0.21	0.22	0.12	0.29	0.15	0.28	0.16	0.22	0.19	0.08	0.29
Er_2O_3	0.41	0.37	0.43	0.33	0.38	0.42	0.47	0.21	0.30	0.23	0.39	0.35
Tm_2O_3	- - -	- - -	- - -	- - -	- - -	- - -	- - -	- - -	- - -	- - -	- - -	- - -
Yb_2O_3	0.23	0.13	0.20	0.16	0.23	0.19	0.22	0.14	0.12	0.17	0.16	0.09
Lu_2O_3	- - -	- - -	- - -	- - -	- - -	- - -	- - -	- - -	- - -	- - -	- - -	- - -
PbO	- - -	0.15	- - -	0.17	- - -	- - -	- - -	- - -	- - -	0.28	- - -	- - -
ThO_2	34.03	33.23	33.94	33.08	31.79	34.91	34.05	34.78	33.58	31.53	33.60	32.95
UO_2	2.12	0.99	0.86	0.76	3.18	1.77	1.53	0.77	0.80	0.78	0.87	0.74
F	1.37	1.08	1.69	1.11	1.04	1.15	1.24	0.64	1.15	1.46	1.09	1.05
−O ≡ F	0.58	0.45	0.71	0.47	0.44	0.48	0.52	0.27	0.49	0.62	0.46	0.44
Total	90.87	86.47	91.06	88.31	87.22	88.51	88.72	88.85	88.43	85.21	88.26	88.89
*H_2O	9.13	13.53	8.94	11.69	12.78	11.49	11.28	11.15	11.57	14.79	11.74	11.11

Notes: Brockite compositons are determined by EPMA. Results are not converted to atoms per formula unit as the structure and H_2O/OH^- content remain undetermined. Tm_2O_3 and Lu_2O_3 were analyzed but routinely below detection limit. The presence of ferric iron, reduced sulfur, and hexavalent uranium will have marginal affect on calcualted compositons. *H_2O calculated by difference; - - -: below detection limit.

Table 1b. Analyses of unnamed intermediate brockite-vanadate solid solution

	broV-1	broV-2	broV-3	broV-4	broV-4b	broV-5	broV-6	broV-6b	broV-6c	broV-7	broV-7b
SiO_2	0.63	0.46	0.46	0.81	0.72	0.45	0.49	0.38	0.48	0.61	0.68
P_2O_5	9.59	12.18	15.11	8.95	8.35	9.93	14.62	11.23	11.16	7.83	8.59
SO_3	0.23	0.17	0.24	0.25	0.20	0.24	0.18	0.22	0.16	0.26	0.16
V_2O_5	17.56	15.03	11.66	19.52	19.84	18.73	12.27	17.29	15.01	19.73	18.48
CaO	9.78	10.30	12.02	11.08	10.98	10.33	10.46	10.54	9.67	10.92	10.29
FeO	1.38	0.29	1.95	0.36	0.39	0.11	0.31	0.31	0.96	1.26	0.70
SrO	0.10	0.22	0.39	0.13	0.09	0.12	0.30	0.17	0.22	0.08	0.05
BaO	- - -	0.19	0.42	0.11	- - -	0.05	0.33	0.14	0.26	0.05	0.09
Y_2O_3	6.40	6.06	4.77	4.71	4.52	6.81	5.62	4.84	5.74	4.68	4.55
La_2O_3	0.06	0.08	0.14	0.11	0.08	0.11	0.14	0.12	0.09	0.07	0.06
Ce_2O_3	0.79	0.53	0.36	0.65	0.63	0.61	0.30	0.47	0.36	0.51	0.49
Pr_2O_3	- - -	- - -	- - -	- - -	- - -	- - -	- - -	0.10	- - -	- - -	0.10
Nd_2O_3	0.14	0.29	0.26	0.26	0.28	0.20	0.22	0.18	0.18	0.19	0.30
Sm_2O_3	0.28	0.37	0.38	0.28	0.29	0.26	0.24	0.37	0.19	0.16	0.35
Eu_2O_3	0.26	0.34	0.28	0.30	0.19	0.28	0.26	0.27	0.26	0.21	0.18
Gd_2O_3	1.11	1.39	1.28	1.17	1.07	1.07	1.24	1.32	1.06	0.91	0.91
Tb_2O_3	0.26	0.25	0.26	0.23	0.19	0.21	0.28	0.25	0.27	0.18	0.16
Dy_2O_3	1.92	2.13	1.97	1.76	1.67	1.93	2.08	1.90	1.94	1.69	1.72
Ho_2O_3	0.31	0.32	0.24	0.36	0.23	0.18	0.20	0.22	0.27	0.27	0.34
Er_2O_3	0.52	0.56	0.50	0.40	0.46	0.53	0.51	0.41	0.56	0.41	0.35
Tm_2O_3	- - -	- - -	- - -	- - -	- - -	- - -	- - -	- - -	- - -	- - -	- - -
Yb_2O_3	0.38	0.20	0.21	0.22	0.26	0.33	0.19	0.16	0.24	0.24	0.19
Lu_2O_3	- - -	- - -	- - -	- - -	- - -	- - -	- - -	- - -	- - -	- - -	- - -
PbO	0.56	0.40	- - -	0.47	0.32	0.48	- - -	0.44	0.28	0.60	0.38
ThO_2	38.30	37.41	36.13	40.06	40.61	39.57	36.11	38.81	34.22	39.73	42.15
UO_2	1.05	1.01	0.82	1.01	1.08	1.07	1.02	1.03	0.96	1.05	1.02
F	2.09	1.91	1.22	1.77	1.89	1.83	2.07	1.57	1.87	1.59	2.03
$-O \equiv F$	0.88	0.80	0.51	0.74	0.79	0.77	0.87	0.66	0.79	0.67	0.86
Total	92.82	91.32	90.55	94.22	93.54	94.69	88.58	92.10	85.61	92.57	93.47
$*H_2O$	7.18	8.68	9.45	5.78	6.46	5.31	11.42	7.90	14.39	7.43	6.53

This is a preprint, the final version is subject to change, of the American Mineralogist (MSA)
Cite as Authors (Year) Title. American Mineralogist, in press.
(DOI will not work until issue is live.) DOI: http://dx.doi.org/10.2138/am-2016-5532

Table 2. Representative analyses of conmplex xenotime-(Y) outgrowths/overgrowths at the CHO and adjacent sandstone

	xenotime-(Y) overgrowths from CHO with alternating porous, hydrated banding													
	xog-21	xog-20	xog-7	xog-25	xog-19	xog-3	xog-22	xog-16	xog-11	xog-30	xog-5	xog-27	xog-12	xog-10
SiO_2	0.60	0.38	0.63	2.86	3.49	0.36	0.80	0.46	0.33	0.45	0.36	0.46	0.36	0.32
P_2O_5	27.22	27.45	27.99	26.99	25.79	25.30	27.09	28.57	28.24	26.56	28.42	24.02	25.58	27.03
SO_3	0.23	0.26	0.13	0.07	0.12	0.27	0.10	0.02	0.02	0.08	0.06	0.18	0.11	0.16
V_2O_5	0.60	0.47	0.35	0.87	0.72	0.95	0.58	0.38	0.39	0.85	0.37	0.63	0.55	0.43
CaO	4.27	4.09	3.28	3.42	3.78	5.47	3.77	2.56	2.02	4.09	3.12	5.01	3.55	3.34
FeO	0.42	0.33	0.21	0.13	0.29	0.26	0.17	0.07	0.04	0.08	0.09	0.30	0.13	0.12
BaO	0.08	0.07	0.10	0.17	0.11	0.11	0.12	0.13	0.11	0.11	0.11	0.09	0.10	0.07
Y_2O_3	40.37	40.53	39.90	36.67	35.62	33.77	35.79	38.43	36.89	33.51	34.19	33.93	34.12	32.60
Nd_2O_3	- - -	- - -	- - -	- - -	- - -	- - -	- - -	- - -	- - -	- - -	- - -	- - -	- - -	- - -
Sm_2O_3	0.13	0.15	0.14	0.13	0.10	0.12	0.13	0.09	0.15	0.13	0.11	0.15	0.13	0.05
Eu_2O_3	0.18	0.23	0.14	0.20	0.18	0.22	0.18	0.15	0.17	0.19	0.19	0.12	0.20	0.10
Gd_2O_3	1.53	1.92	1.24	1.76	1.18	1.77	1.36	1.27	1.53	1.44	1.39	1.25	1.36	1.02
Tb_2O_3	0.56	0.64	0.48	0.67	0.51	0.58	0.47	0.43	0.55	0.49	0.46	0.41	0.54	0.41
Dy_2O_3	4.92	5.22	4.47	5.52	4.53	5.18	4.49	4.14	4.63	4.32	4.06	4.03	4.21	3.39
Ho_2O_3	0.94	1.03	0.89	1.19	1.04	1.05	0.88	1.27	0.95	0.88	0.91	0.78	0.96	0.86
Er_2O_3	2.56	2.75	2.71	2.91	2.99	2.64	2.41	2.42	2.54	2.17	2.15	2.07	2.29	1.95
Tm_2O_3	0.31	0.24	0.45	0.33	0.41	0.23	0.33	0.32	0.37	0.33	0.39	0.21	0.29	0.44
Yb_2O_3	1.72	1.96	2.03	2.08	2.57	1.88	1.79	1.75	1.81	1.49	1.59	1.43	1.72	1.47
Lu_2O_3	0.13	0.18	0.22	0.21	0.28	0.17	0.16	0.24	0.17	0.16	0.20	0.13	0.13	0.25
PbO	- - -	- - -	0.45	- - -	0.14	- - -	0.39	- - -	0.39	0.38	0.35	0.23	0.19	0.41
ThO_2	7.30	5.38	4.59	4.34	4.36	7.42	5.82	3.91	4.48	6.49	4.46	7.51	4.31	4.26
UO_2	0.84	0.80	0.96	0.83	1.29	0.81	0.82	0.62	0.80	0.66	0.88	0.72	0.90	0.92
F	2.32	2.21	2.60	2.22	2.64	3.01	2.44	2.52	2.53	2.51	2.28	2.62	3.02	2.82
$-O \equiv F$	0.98	0.93	1.10	0.93	1.11	1.27	1.03	1.06	1.07	1.06	0.96	1.10	1.27	1.19
Total	96.24	95.39	92.86	92.66	91.02	90.31	89.09	88.69	88.04	86.33	85.17	85.18	83.49	81.23
$*H_2O$	3.76	4.61	7.14	7.34	8.98	9.69	10.91	11.31	11.96	13.67	14.83	14.82	16.51	18.77

Notes: Xenotime-(Y) compositons determined by EPMA are presented in order of increasing H_2O (increasingly low totals). Results are not converted to atoms per formula unit as compositons represent alternating xenotime-(Y) and porous zones which contain excess H_2O or OH^- and may represent a distinct hydrated Th-Ca phase. SrO, La_2O_3, Ce_2O_3, Pr_2O_3 were analyzed but below detection limit. The presence of ferric iron, reduced sulfur, and hexavalent uranium will have a marginal affect on calcualted compositons. $*H_2O$ calculated by difference; - - -: below detection limit.

This is a preprint, the final version is subject to change, of the American Mineralogist (MSA)
Cite as Authors (Year) Title. American Mineralogist, in press.
(DOI will not work until issue is live.) DOI: http://dx.doi.org/10.2138/am-2016-5532

Table 2. ***continued***

	low H_2O domains of xenotime-(Y) overgrowths						sandstone-hosted xenotime-(Y) outgrowths			
	xog-17	xog-17b	xog-6	xog-7b	xog-3b	xog-6b	sxog-1	sxog-2	sxog-9	sxog-10
SiO_2	0.25	0.40	0.75	0.53	0.45	0.21	1.09	2.78	9.78	4.94
P_2O_5	31.63	30.95	30.05	33.37	28.98	30.49	32.05	28.35	27.59	28.76
SO_3	0.09	0.01	0.17	0.01	0.02	0.04	0.03	0.05	0.02	0.07
V_2O_5	0.34	0.02	0.31	0.03	0.53	0.16	- - -	0.27	- - -	0.19
CaO	1.91	1.00	2.14	0.89	2.85	2.91	1.31	2.19	1.05	1.97
FeO	0.29	0.09	0.07	0.07	0.02	0.07	0.07	0.11	3.13	0.60
BaO	0.10	0.06	0.11	0.11	0.07	0.08	0.08	0.07	0.11	0.09
Y_2O_3	46.42	46.63	43.99	49.97	42.81	44.53	43.96	39.96	38.91	40.23
Nd_2O_3	- - -	- - -	- - -	- - -	- - -	- - -	0.11	0.12	0.05	- - -
Sm_2O_3	0.02	0.09	0.02	0.03	0.10	0.02	0.11	0.12	0.06	0.06
Eu_2O_3	0.04	0.13	0.12	0.06	0.18	0.06	0.16	0.10	0.03	0.14
Gd_2O_3	0.51	1.15	1.45	0.96	1.41	0.46	1.44	1.40	0.72	1.28
Tb_2O_3	0.36	0.50	0.52	0.50	0.54	0.31	0.63	0.67	0.32	0.57
Dy_2O_3	4.43	5.27	5.06	5.04	5.47	4.11	5.48	5.53	3.93	5.14
Ho_2O_3	1.20	1.16	1.10	1.18	1.20	1.19	1.17	1.12	0.93	1.07
Er_2O_3	4.15	3.11	2.97	3.24	3.19	3.97	3.31	3.11	3.26	2.90
Tm_2O_3	0.45	0.29	0.33	0.29	0.31	0.55	0.35	0.35	0.12	0.27
Yb_2O_3	3.59	2.05	2.16	2.30	2.26	3.65	2.33	2.40	2.88	2.15
Lu_2O_3	0.42	0.20	0.24	0.27	0.23	0.38	0.28	0.20	0.35	0.28
PbO	0.16	- - -	- - -	- - -	- - -	- - -	- - -	- - -	- - -	- - -
ThO_2	3.30	2.42	3.99	1.76	4.04	2.91	2.15	3.32	1.36	2.31
UO_2	1.20	0.47	0.76	0.48	0.55	1.31	0.53	0.82	0.78	0.71
F	2.08	2.05	2.23	1.96	2.84	2.43	1.83	2.11	0.98	1.84
$-O \equiv F$	0.88	0.86	0.94	0.83	1.20	1.02	0.77	0.89	0.41	0.77
Total	102.03	97.19	97.59	102.22	96.86	98.79	97.67	94.28	95.95	94.80
$*H_2O$	- - -	2.81	2.41	- - -	3.14	1.21	2.33	5.72	4.05	5.20

This is a preprint, the final version is subject to change, of the American Mineralogist (MSA)
Cite as Authors (Year) Title. American Mineralogist, in press.
(DOI will not work until issue is live.) DOI: http://dx.doi.org/10.2138/am-2016-5532

Table 3. LA-ICP-MS trace element data from fluorites throughout the BLAC

Sample #:	12BL23		13BL09		12BL33		R11-32		R11-32		WBD10-475		S121-945	
Mineral:	fluorite		fluorite		fluorite		fluorite		fluorite		fluorite		fluorite	
Description:	Cole HFSE(+HREE) occurrence		additonal vein at CHO		karst cavity filling in Mississippian limestone		inclusion-rich hydrothermal veining		inclusion-poor hydrothermal veining		REE-poor carbonatite		carbonate vein carbonatite?	
	n=11	1σ	n=8	1σ	n=9	1σ	n=6	1σ	n=6	1σ	n=12	1σ	n=9	1σ
Ca (wt.%)*	48.27	0.48	49.39	0.26	49.71	0.26	49.16	0.12	49.22	0.19	49.02	0.64	48.92	0.32
Sr (ppm)	6049.7	1982.5	113.7	31.9	218.7	208.5	2984.3	187.2	2573.9	1240.3	13152.9	2422.8	5789.9	3050.6
Y	95.7	50.9	92.9	34.7	41.5	26.3	123.4	12.3	93.3	31.0	22.9	10.2	43.5	22.5
La	1.1	1.0	10.9	9.5	9.2	4.6	15.6	4.3	5.4	1.9	8.8	4.8	3.7	3.6
Ce	1.8	1.7	25.5	18.9	16.6	8.0	39.9	10.5	15.7	5.1	21.5	10.7	8.7	7.5
Pr	0.2	0.2	3.1	2.1	2.5	1.1	7.0	1.9	3.3	1.3	3.8	1.9	1.5	1.1
Nd	0.7	0.9	13.3	8.8	12.1	5.0	40.9	9.9	21.2	8.6	16.9	7.7	8.6	5.2
Sm	1.3	0.5	3.2	1.5	3.2	1.5	10.3	2.9	5.7	2.6	3.2	1.1	2.6	1.6
Eu	0.9	0.5	1.0	0.5	1.1	0.6	2.3	0.4	1.4	0.6	0.8	0.3	0.9	0.7
Gd	6.2	2.6	4.5	2.2	4.2	2.3	11.4	2.3	6.9	2.8	2.1	1.0	3.5	2.3
Tb	1.8	0.8	0.9	0.4	0.6	0.4	1.3	0.4	0.7	0.3	0.2	0.2	0.4	0.3
Dy	14.5	7.6	6.8	3.4	3.7	2.4	6.5	1.1	4.4	1.7	0.8	0.8	2.7	2.2
Ho	2.9	1.6	1.5	0.7	0.7	0.5	1.5	0.3	0.9	0.3	0.2	0.1	0.5	0.3
Er	7.3	3.9	4.6	2.2	1.6	1.1	3.6	1.0	2.3	0.8	bdl	- - -	0.8	1.0
Tm	0.9	0.5	0.6	0.4	0.2	0.1	0.3	0.0	0.2	0.1	bdl	- - -	0.1	0.1
Yb	4.7	2.4	3.6	2.3	1.0	0.8	1.1	0.2	0.9	0.3	bdl	- - -	0.6	0.5
Lu	0.5	0.3	0.5	0.3	0.1	0.1	0.1	0.0	0.1	0.0	bdl	- - -	bdl	- - -
Th	36.5	27.2	8.4	9.8	1.3	1.5	bdl	0.2	0.2	0.3	bdl	- - -	bdl	- - -
U	13.1	5.3	2.8	2.9	0.4	0.5	0.2	0.1	0.1	0.1	bdl	- - -	0.1	0.1
Y/Ho	33.2		62.4		58.6		84.9		102.5		95.9		89.3	

Notes: *Ca concentration obtained by electron microprobe and reported in elemental weight percent. All other elements reported in ppm. n = number of averaged analyses.

This is a preprint, the final version is subject to change, of the American Mineralogist (MSA)
Cite as Authors (Year) Title. American Mineralogist, in press.
(DOI will not work until issue is live.) DOI: http://dx.doi.org/10.2138/am-2016-5532

Table 4. Results of in-situ LA-ICP-MS U-Pb geochronology

		Isotopic Ratios and Errors						Ages					
Sample-spot	Mineral/rock	$^{207}Pb/^{235}U$	±2σ	$^{206}Pb/^{238}U$	±2σ	$^{207}Pb/^{206}Pb$	±2σ	$^{207}Pb/^{235}U$	±2σ (Ma)	$^{206}Pb/^{238}U$	±2σ (Ma)	$^{207}Pb/^{206}Pb$	±2σ (Ma)
CF7100V-14	zircon/CHO	2.09108	0.06288	0.13524	0.00319	0.11215	0.00164	1145.9	20.6	817.7	18.1	1834.6	26.4
CF7100V-15	zircon/CHO	1.16770	0.10156	0.07440	0.00636	0.11384	0.00189	785.6	47.0	462.6	38.1	1861.6	29.8
CF7100V-24	zircon/CHO	2.02358	0.06835	0.12774	0.00348	0.11490	0.00188	1123.5	22.8	774.9	19.9	1878.3	29.3
CF7100V-23	zircon/CHO	5.35553	0.23195	0.34583	0.01280	0.11232	0.00220	1877.8	36.7	1914.6	61.2	1837.3	35.3
CF7100V-26	zircon/CHO	4.69427	0.13766	0.30026	0.00685	0.11339	0.00163	1766.2	24.4	1692.6	33.9	1854.5	25.9
CF7100V-31	zircon/CHO	5.05434	0.12903	0.32314	0.00532	0.11345	0.00176	1828.5	21.5	1805.1	25.9	1855.4	27.8
CF7100V-18	zircon/CHO	5.66530	0.16380	0.34029	0.00671	0.12075	0.00211	1926.1	24.8	1888.1	32.2	1967.4	31.0
CF7100V-12	zircon/CHO	7.13619	0.17248	0.39987	0.00624	0.12944	0.00184	2128.6	21.4	2168.4	28.7	2090.4	24.9
CF7100V-13	zircon/CHO	7.23483	0.16721	0.40172	0.00588	0.13063	0.00176	2140.8	20.5	2176.9	27.0	2106.4	23.5
CF7100V-21	zircon/CHO	12.06146	0.39979	0.49729	0.01397	0.17592	0.00239	2609.2	30.8	2602.1	60.0	2614.8	22.5
CF7100V-17	zircon/CHO	14.04836	0.34929	0.53573	0.00911	0.19020	0.00263	2753.0	23.4	2765.6	38.2	2743.9	22.6
CF7100V-30	zircon/CHO	13.56289	0.35036	0.51532	0.00942	0.19090	0.00267	2719.7	24.3	2679.3	40.0	2749.9	22.9
Staatz (1983)	zircon/granite	n.a.	n.a.	n.a.	n.a.	n.a.	n.a.	939.00	n.a.	389.00	n.a.	2628.00	n.a.

This is a preprint, the final version is subject to change, of the American Mineralogist (MSA)
Cite as Authors (Year) Title. American Mineralogist, in press.
(DOI will not work until issue is live.) DOI: http://dx.doi.org/10.2138/am-2016-5532

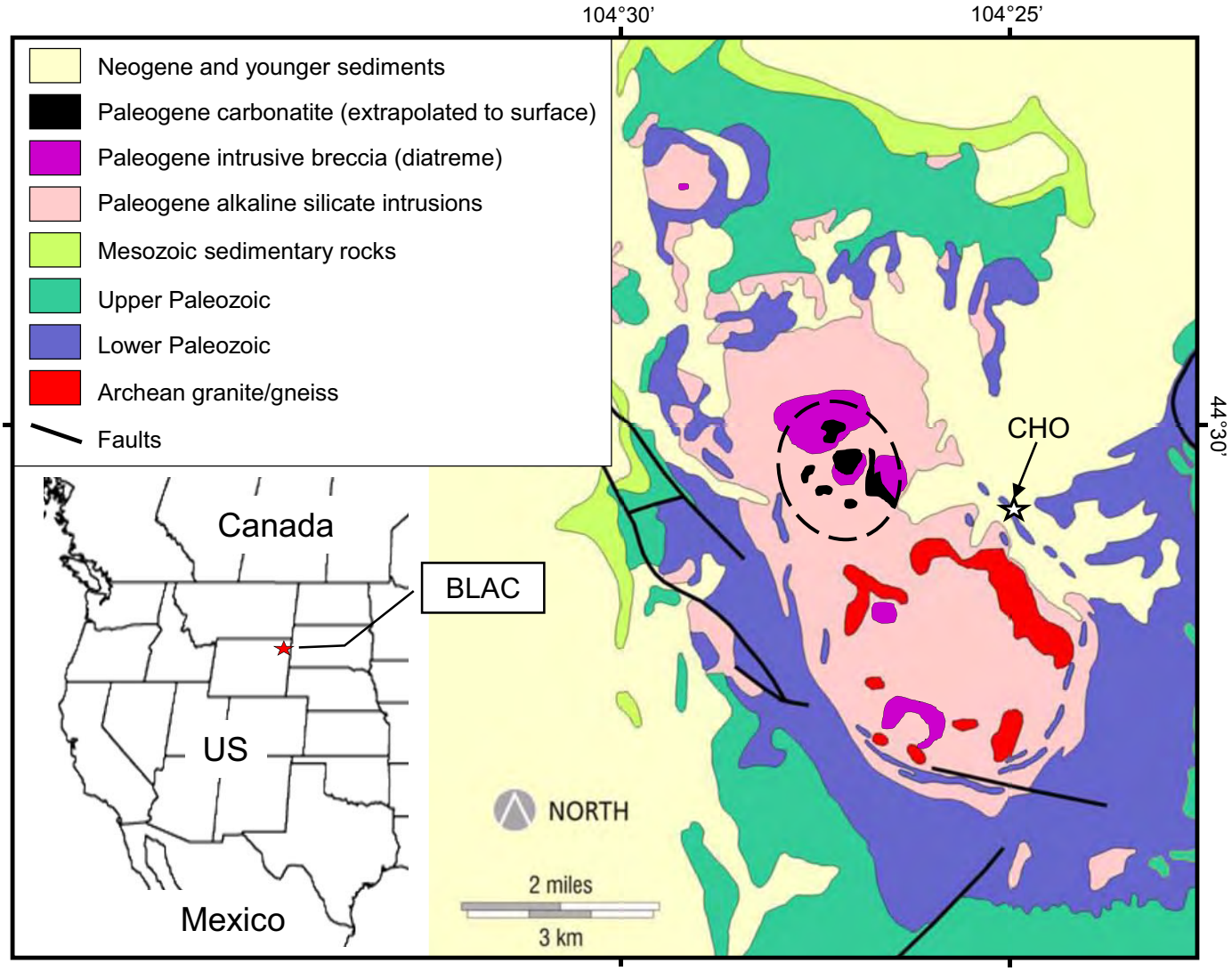

Figure 1.

This is a preprint, the final version is subject to change, of the American Mineralogist (MSA)
Cite as Authors (Year) Title. American Mineralogist, in press.
(DOI will not work until issue is live.) DOI: http://dx.doi.org/10.2138/am-2016-5532

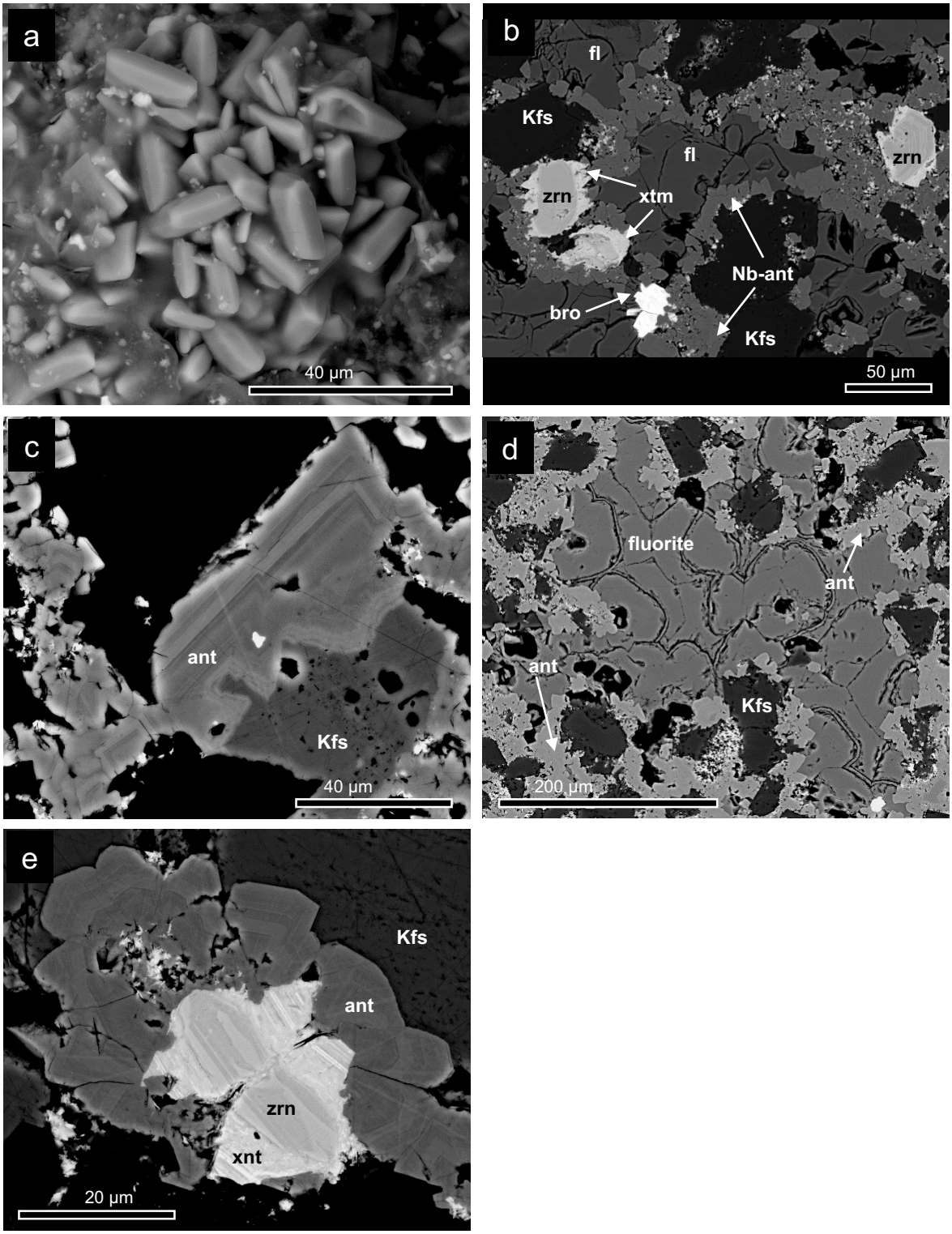

Figure 2.

This is a preprint, the final version is subject to change, of the American Mineralogist (MSA)
Cite as Authors (Year) Title. American Mineralogist, in press.
(DOI will not work until issue is live.) DOI: http://dx.doi.org/10.2138/am-2016-5532

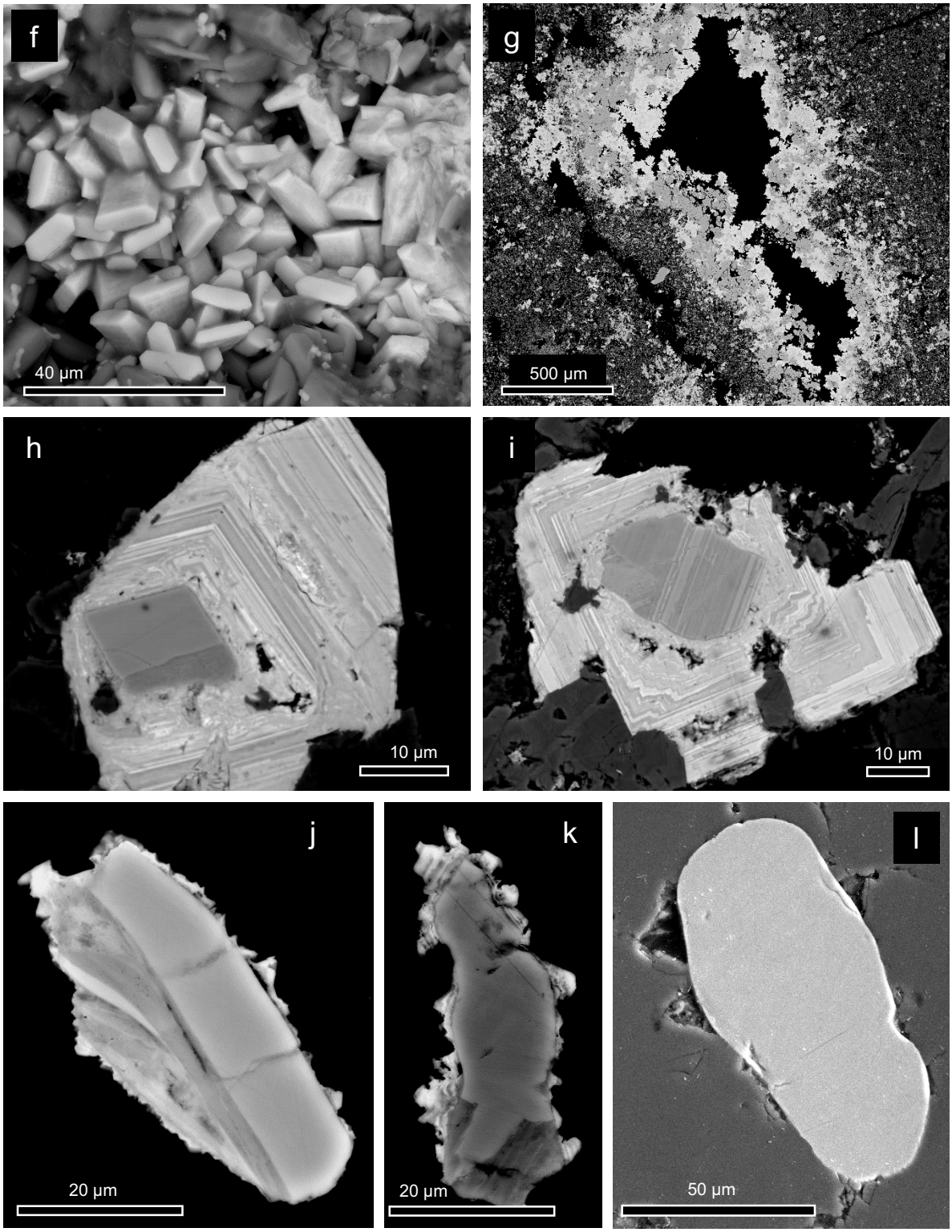

Figure 2. continued

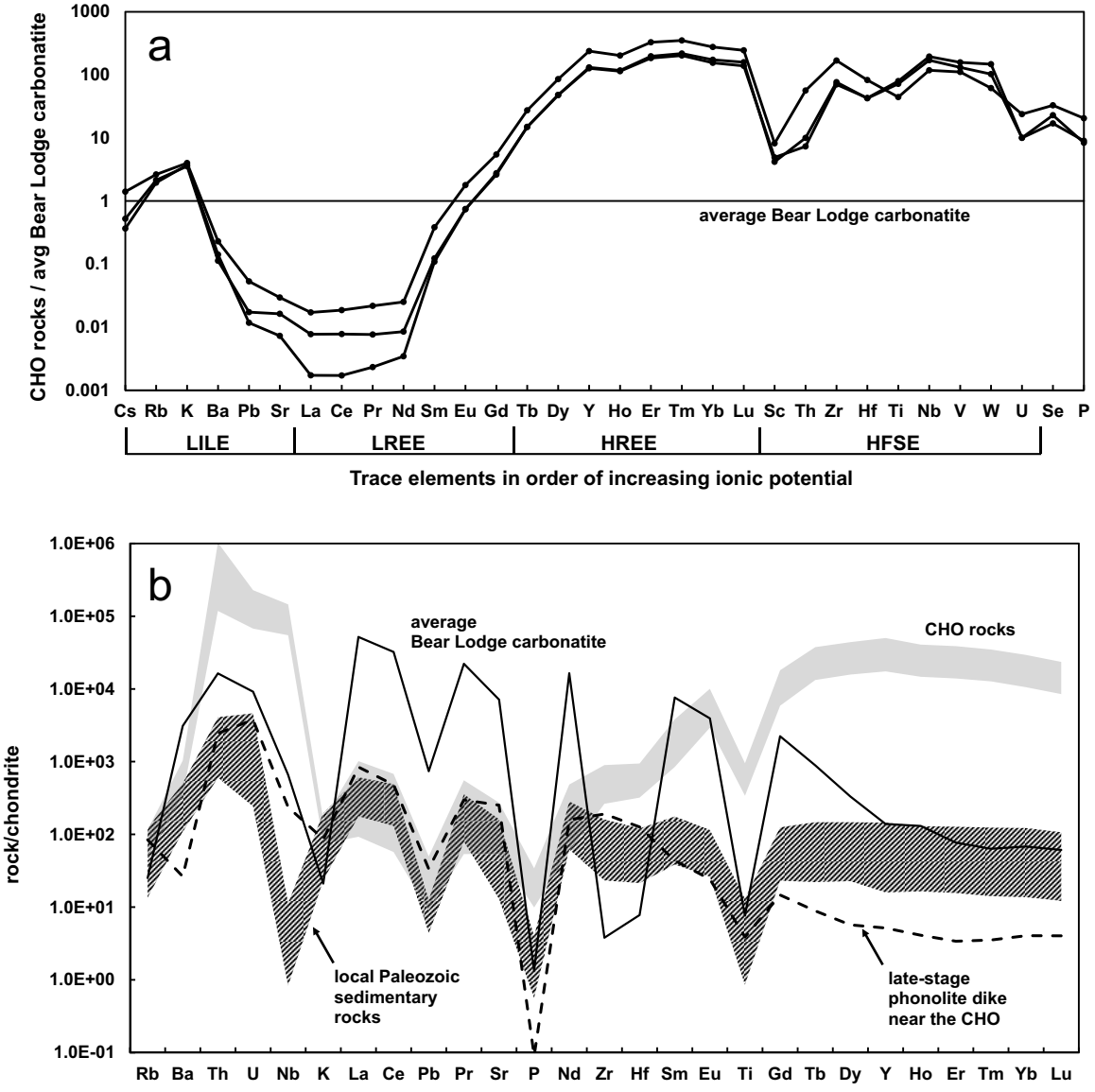
a
CHO rocks / avg Bear Lodge carbonatite
1000
100
10
1
0.1
0.01
0.001
average Bear Lodge carbonatite
Cs Rb K Ba Pb Sr La Ce Pr Nd Sm Eu Gd Tb Dy Y Ho Er Tm Yb Lu Sc Th Zr Hf Ti Nb V W U Se P
LILE
LREE
HREE
HFSE
Trace elements in order of increasing ionic potential
b
rock/chondrite
1.0E+06
1.0E+05
1.0E+04
1.0E+03
1.0E+02
1.0E+01
1.0E+00
1.0E-01
average
Bear Lodge carbonatite
CHO rocks
local Paleozoic
sedimentary
rocks
late-stage
phonolite dike
near the CHO
Rb Ba Th U Nb K La Ce Pb Pr Sr P Nd Zr Hf Sm Eu Ti Gd Tb Dy Y Ho Er Tm Yb Lu

Figure 3.

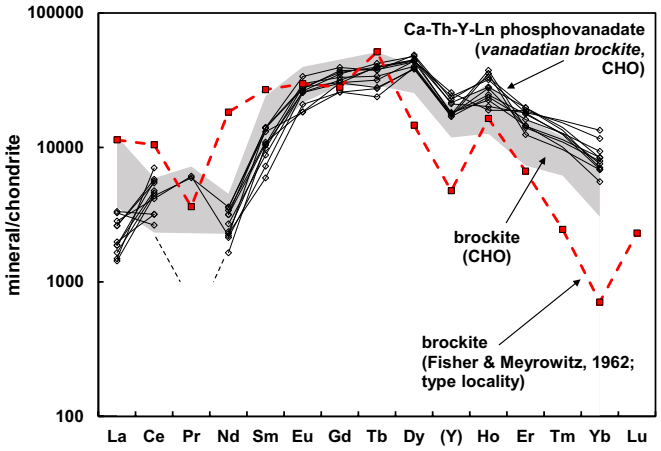
100000
10000
1000
100
mineral/chondrite
La Ce Pr Nd Sm Eu Gd Tb Dy (Y) Ho Er Tm Yb Lu
Ca-Th-Y-Ln phosphovanadate
(*vanadatian brockite*,
CHO)
brockite
(CHO)
brockite
(Fisher & Meyrowitz, 1962;
type locality)

Figure 4.

This is a preprint, the final version is subject to change, of the American Mineralogist (MSA)
Cite as Authors (Year) Title. American Mineralogist, in press.
(DOI will not work until issue is live.) DOI: http://dx.doi.org/10.2138/am-2016-5532

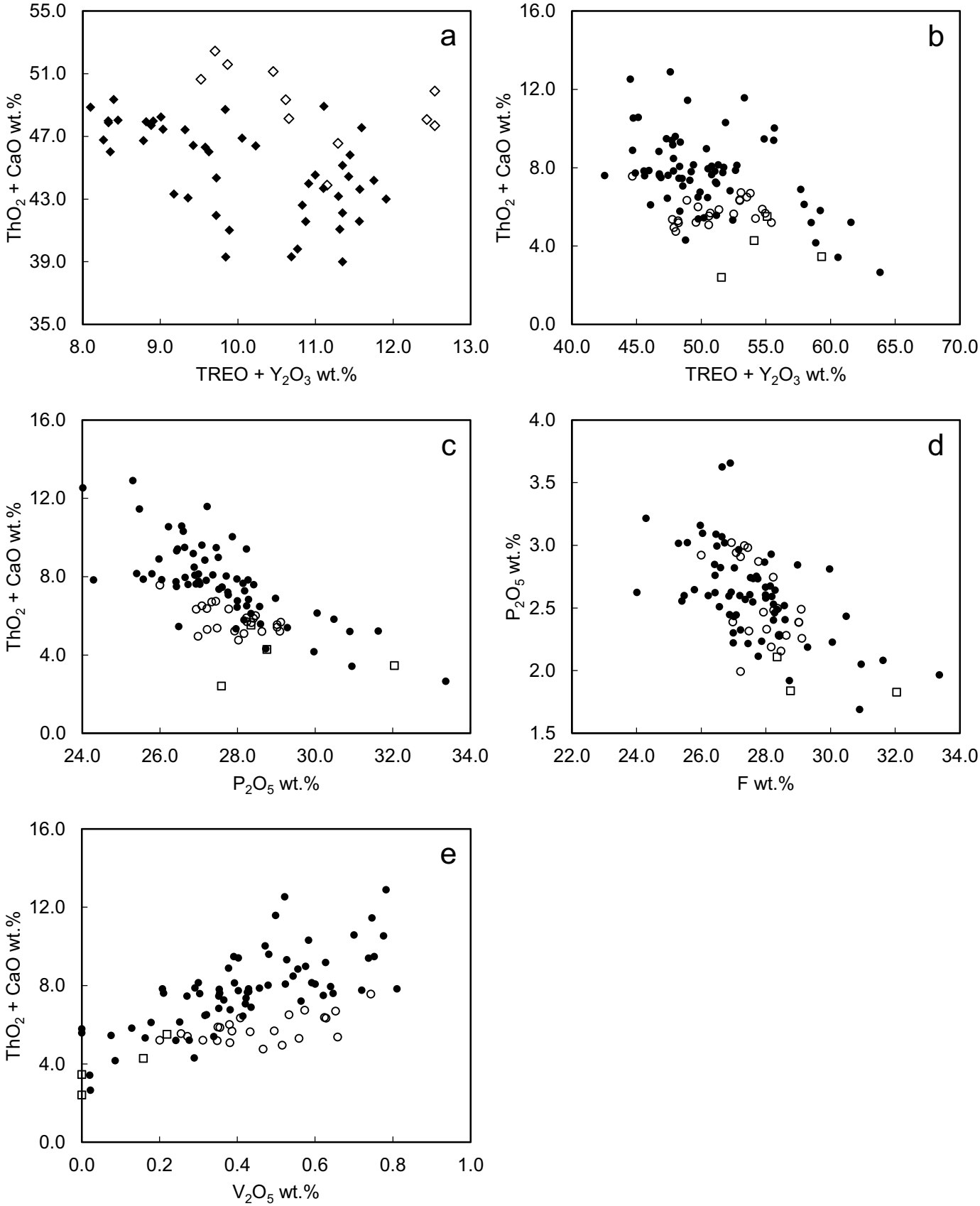

Figure 5.

This is a preprint, the final version is subject to change, of the American Mineralogist (MSA)
Cite as Authors (Year) Title. American Mineralogist, in press.
(DOI will not work until issue is live.) DOI: http://dx.doi.org/10.2138/am-2016-5532

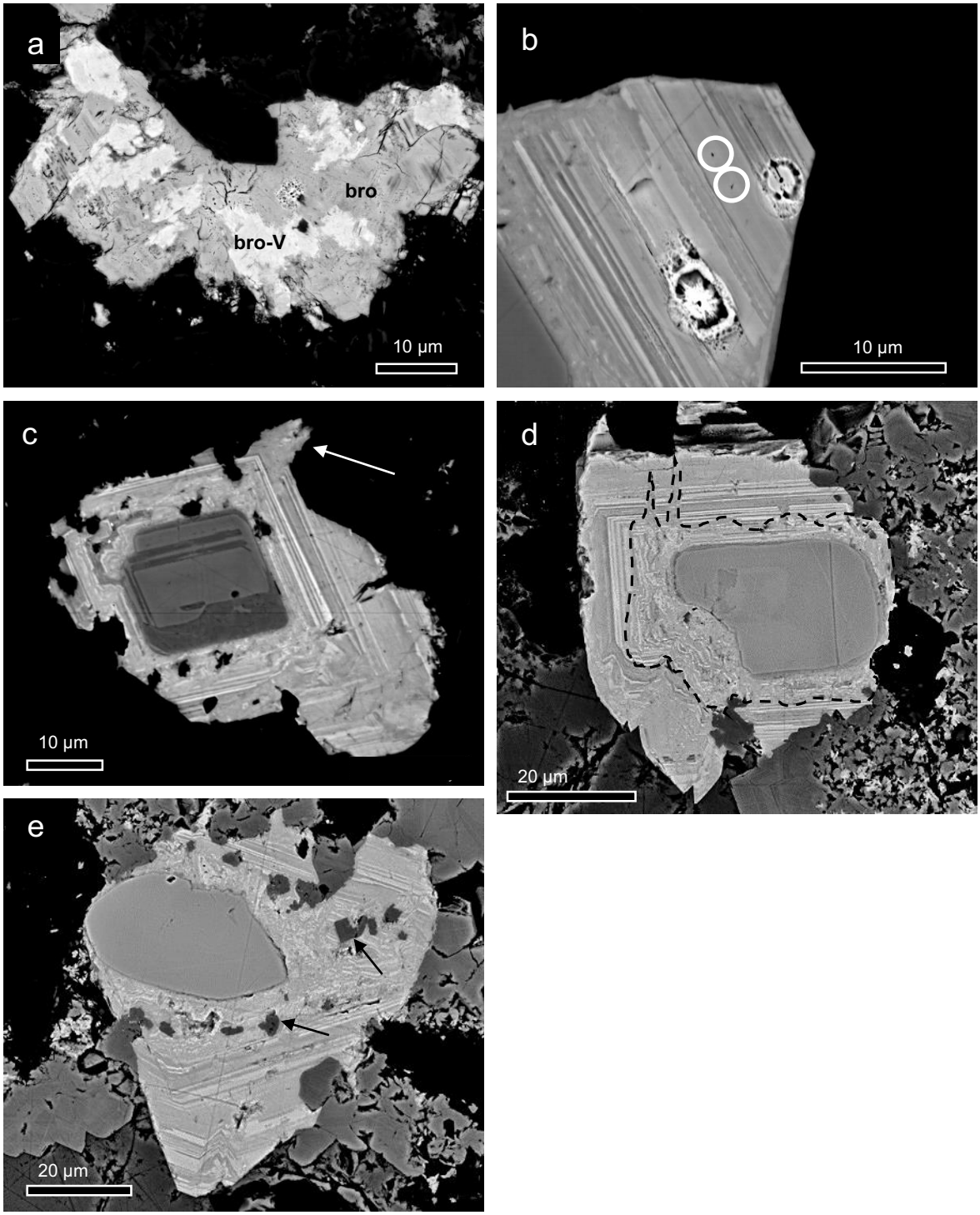

Figure 6.

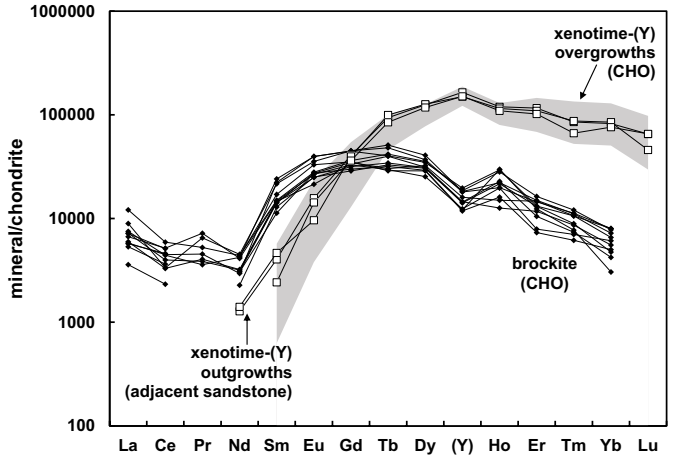
1000000
100000
10000
1000
100
mineral/chondrite
xenotime-(Y)
overgrowths
(CHO)
brockite
(CHO)
xenotime-(Y)
outgrowths
(adjacent sandstone)
La Ce Pr Nd Sm Eu Gd Tb Dy (Y) Ho Er Tm Yb Lu

Figure 7.

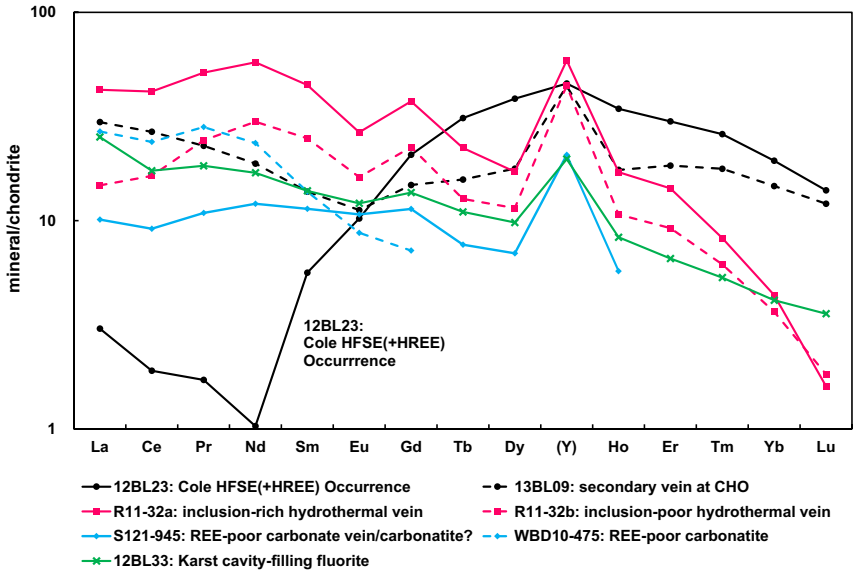
100
10
1
mineral/chondrite
12BL23:
Cole HFSE(+HREE)
Occurrrence
La
Ce
Pr
Nd
Sm
Eu
Gd
Tb
Dy
(Y)
Ho
Er
Tm
Yb
Lu
12BL23: Cole HFSE(+HREE) Occurrence
13BL09: secondary vein at CHO
R11-32a: inclusion-rich hydrothermal vein
R11-32b: inclusion-poor hydrothermal vein
S121-945: REE-poor carbonate vein/carbonatite?
WBD10-475: REE-poor carbonatite
12BL33: Karst cavity-filling fluorite

Figure 8.

This is a preprint, the final version is subject to change, of the American Mineralogist (MSA)
Cite as Authors (Year) Title. American Mineralogist, in press.
(DOI will not work until issue is live.) DOI: http://dx.doi.org/10.2138/am-2016-5532

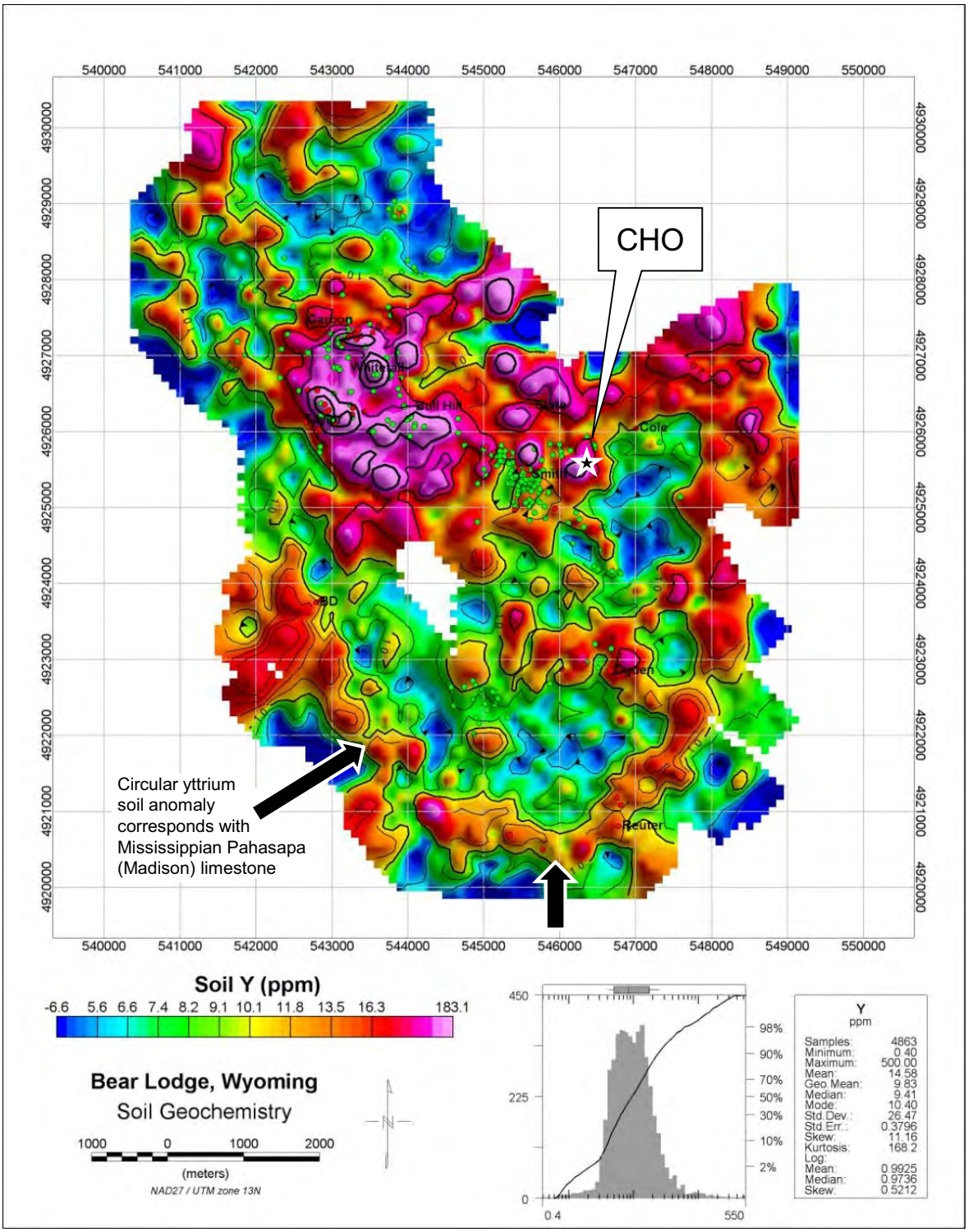

Figure 9.